Ecological Indicators 186 (2026) 114875

Contents lists available at ScienceDirect

Ecological Indicators

journal homepage: www.elsevier.com/locate/ecolind

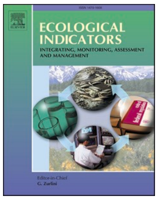

Identifying soil moisture thresholds for agricultural drought sensitivity through coupling modeled and satellite data in a humid temperate catchment

Abdul Baqi Ahady [*], Stefanie Wolf, Elena-Maria Klopries

Institute of Hydraulic Engineering and Water Resources Management, RWTH Aachen University, 52074 Aachen, Germany

ARTICLE INFO

Keywords:
Agricultural drought
Soil moisture
Vegetation condition index (VCI)
Soil moisture thresholds
Rur catchment

ABSTRACT

Agricultural drought assessment requires understanding the conditions under which soil moisture (SM) deficits translate into measurable vegetation stress. This study presents a geospatial, threshold-driven framework to assess agricultural drought vulnerability by coupling modeled SM with the satellite-derived Vegetation Condition Index (VCI) in the Rur catchment, western Germany (2000–2024). Long-term SM observations and VCI data were aggregated to a common spatiotemporal scale and standardized using *Z*-scores to identify relative drought anomalies. An optimal SM threshold of $\leq$64% nFK (available field capacity) was then identified to discriminate water-limited from energy-limited conditions, resulting in a substantial improvement in SM–VCI coupling from $r = 0.109$ to 0.354 (+225%), corresponding to an increase in explained variance from 1.2% to 12.5%. Under these conditions, a dynamic seasonal pattern emerged, with water-limited areas expanding from the northern agricultural lowlands in May–June to the entire catchment by July, and peak coupling occurring in August (mean $r = 0.501$). Spatially, relatively strong correlations ($r > 0.50$) were concentrated in agricultural and grassland areas, whereas forests, particularly in the early summer, showed persistent decoupling. This regime-specific sensitivity provides an ecologically informed basis for drought monitoring, with agricultural land and grasslands being most responsive. These findings demonstrate that effective drought monitoring in humid catchments requires first diagnosing ecologically meaningful water-limited regimes using locally defined SM thresholds and then focusing on moisture-sensitive land-use types. This regime-aware, spatially explicit framework provides an actionable foundation for targeted drought management in heterogeneous humid temperate landscapes.

List of Abbreviation

DWD	Deutscher Wetterdienst
EVI	Enhanced Vegetation Index
GEE	Google Earth Engine
IDW	Inverse Distance Weighting
LST	Land Surface Temperature
LOO	Leave One Out
MODIS	Moderate Resolution Imaging Spectroradiometer
NDVI	Normalized Difference Vegetation Index
nFK	Nutzbare Feldkapazität
SM	Soil Moisture
USGS	United States Geological Survey
VCI	Vegetation Condition Index

1. Introduction

Soil moisture (SM) and vegetation dynamics are fundamental components of land–atmosphere interactions and play a critical role in understanding agricultural drought assessment. The interplay between these elements influences crop health and productivity, making their monitoring essential for effective agricultural management (Ahady et al., 2025; Mohanty et al., 2017). SM governs plant available water, regulates energy fluxes, and shapes local plant water availability processes (J. Tian et al., 2019; Wei et al., 2022). Vegetation, in turn, reflects the cumulative effect of soil water availability and atmospheric demand, making it a key indicator of drought impacts and ecosystem stress (Li and Sawada, 2022). Understanding the coupling between SM and vegetation is therefore essential for detecting drought onset, monitoring its progression, and informing mitigation strategies.

---

[*] Corresponding author.
E-mail address: ahady@iww.rwth-aachen.de (A.B. Ahady).

https://doi.org/10.1016/j.ecolind.2026.114875
Received 2 February 2026; Received in revised form 10 April 2026; Accepted 13 April 2026

The importance of this challenge has intensified in recent decades, as central Europe—including Germany—has experienced severe drought events (e.g., 2003, 2018–2022) that have substantially affected agricultural productivity and water resources (Gessner et al., 2023; Luo et al., 2024). These events highlight the vulnerability of even humid temperate regions to increasing drought risk under climate change, underscoring the urgent need for improved monitoring approaches that can detect incipient vegetation stress before irreversible damage occurs.

Yet translating this urgency into effective monitoring remains challenging, as the SM-vegetation relationship is highly complex and nonlinear. Such complexity arises from the dual role of vegetation in soil–atmosphere interactions: while canopy shading and microclimate effects can reduce evaporation, vegetation can simultaneously intensify soil water depletion via transpiration (Ahemd et al., 2016; Wang et al., 2018). Vegetation responses to SM deficits are often lagged, heterogeneous, and modulated by factors such as land cover, rooting depth, and local climate (Li and Sawada, 2022; Liang et al., 2024; van Hateren et al., 2021). This sensitivity of land surface processes to SM is a central parameter in the coupled land-atmosphere system, determining whether ecosystems operate in energy-limited or water-limited regimes (Seneviratne et al., 2010; Teuling et al., 2006). Global and regional studies have identified critical SM thresholds using atmospheric and flux-based proxies, such as evaporative fraction, drying rates, and diurnal temperature ranges, revealing how regime persistence varies across climates (Feldman et al., 2019; Liu et al., 2025), while complementary evidence suggests a widespread shift from energy to water limitation under climate change, driven by increasing radiation and decreasing SM (Denissen et al., 2022). However, these approaches diagnose regime transitions indirectly, through surface flux dynamics or atmospheric feedbacks, rather than through the vegetation response itself.

A more direct diagnostic would assess when SM falls below the absolute threshold at which vegetation health itself becomes limited. This is particularly acute for agricultural drought assessment in humid temperate regions, where water limitation is intermittent rather than chronic (Meng et al., 2022). In such regions, unlike arid and semi-arid systems, moisture–vegetation relationships are strong only during discrete dry windows, a pattern demonstrated globally (Li and Sawada, 2022) and specifically across European ecosystems (Fu et al., 2022a; Stocker et al., 2018). Yet current operational drought monitoring systems, such as the European Drought Observatory (EDO), rely on anomaly-based indicators calibrated at continental scales. While effective for broad-scale assessment, these relative approaches conflate periods of water sufficiency with episodes of genuine stress, obscuring the local heterogeneity that governs vegetation drought sensitivity (Du et al., 2023; Li et al., 2022; Luo et al., 2021; Na et al., 2021; Ruichen et al., 2023; Wei et al., 2022; West et al., 2018; Zhang et al., 2022). Identifying these critical periods is therefore a prerequisite for meaningful agricultural drought assessment in precipitation-rich environments, where seasonally averaged analyses often fail to detect emerging stress signals (Otkin et al., 2018; Seneviratne et al., 2010).

Supporting this concern, continental-scale evidence reveals pronounced asynchrony between SM and vegetation droughts across Europe, with vegetation frequently remaining stable—or even productive—during moderate SM deficits, particularly in humid regions (van Hateren et al., 2021). These findings underscore that SM anomalies do not automatically translate into vegetation stress and have prompted a conceptual shift toward treating SM and vegetation states as distinct but conditionally linked components of agricultural drought. However, while prior studies convincingly document this decoupling, they stop short of providing a framework for determining when and where they actually couple. What remains lacking is an operational framework capable of identifying the local SM threshold at which vegetation transitions into a water-limited regime. This gap is especially critical in heterogeneous landscapes, where the timing and intensity of water limitation vary substantially across soil types, land cover, and topography, with important implications for agriculture and crop protection.

The Rur catchment in western Germany provides an ideal setting to test such an approach. As a long-standing hydrological observatory, it has served as a pilot area for diverse hydrological and ecohydrological research (Ali et al., 2015; Eingrüber and Korres, 2022; Esch et al., 2018; Shukla et al., 2023; Wolf et al., 2023a; Wu et al., 2025). The catchment is characterized by diverse land uses and a temperate climate, making it representative of broader humid temperate regions across central Europe, where soil water content rarely declines to absolute critical thresholds but droughts can still severely affect agricultural production (Pyka et al., 2016; Vidaurre, 2019). Importantly, long-term SM records are available as percentage of usable field capacity (% nFK), an agronomically interpretable measure of plant-available water that avoids the need for index standardization and thereby ensuring a more realistic interpretation of soil–plant water relations.

In this study, we introduce a catchment-scale, data-driven, threshold-based framework to isolate water-limited conditions and quantitatively map SM–vegetation coupling across a heterogeneous humid landscape. Rather than inferring SM thresholds from atmospheric flux proxies, we use vegetation condition itself to define the onset of water limitation. To achieve this, high-resolution, agronomically validated SM data are integrated with the VCI, a normalized satellite-based metric designed to minimize local and seasonal biases in greenness and provide a more robust indicator of relative vegetation stress than raw Normalized Difference Vegetation Index (NDVI; Kogan, 1990).

The specific objectives are to:

- identify the temporal and spatial patterns of SM and vegetation health condition across the Rur catchment;
- determine an optimal SM threshold to isolate water-limited periods and quantify the SM–VCI relationship under these conditions; and
- map the spatial and land-cover-specific sensitivity of vegetation to SM deficits and derive implications for targeted drought monitoring.

This work advances the field in three distinct ways: Methodologically, we provide a reproducible approach for objectively identifying water-limited regimes using vegetation-defined SM thresholds. Empirically, we reveal a dynamic “coupling curtain” that tracks drought propagation across space, time, and land cover types. Operationally, we demonstrate how a locally calibrated threshold transforms theoretical regime separation into a practical tool for regime-specific drought detection in agricultural landscapes. The resulting framework is transferable, offering a refined approach for early agricultural drought detection in humid temperate regions, where water limitation is intermittent, spatially heterogeneous, and often masked by conventional monitoring methods.

2. Data and methods

2.1. Study area

The Rur catchment, a 2354 km^2 sub-catchment of the Meuse River basin, is located predominantly in North Rhine-Westphalia, Germany, with smaller portions extending into Belgium (157 km^2, 6.7%) and the Netherlands (108 km^2, 4.6%) (Bogena et al., 2018; van der Breggen and Hudson, 2024). Topographically, the region slopes from the southern Eifel uplands (~695 m a.s.l.) to the northern loess plains (~24 m a.s.l.), creating distinct environmental gradients (Fig. 1).

Climatic conditions vary considerably across the catchment, reflecting pronounced topographical gradients within a humid temperate climate regime (Döscher et al., 2023). Based on recent observations, mean annual precipitation increases from about 550 mm in the north to 1285 mm in the southwestern uplands (Fig. 2a). Seasonal contrasts are also evident, in the uplands, precipitation is concentrated in winter (November to March; Fig. 2b), contributing to rapid runoff

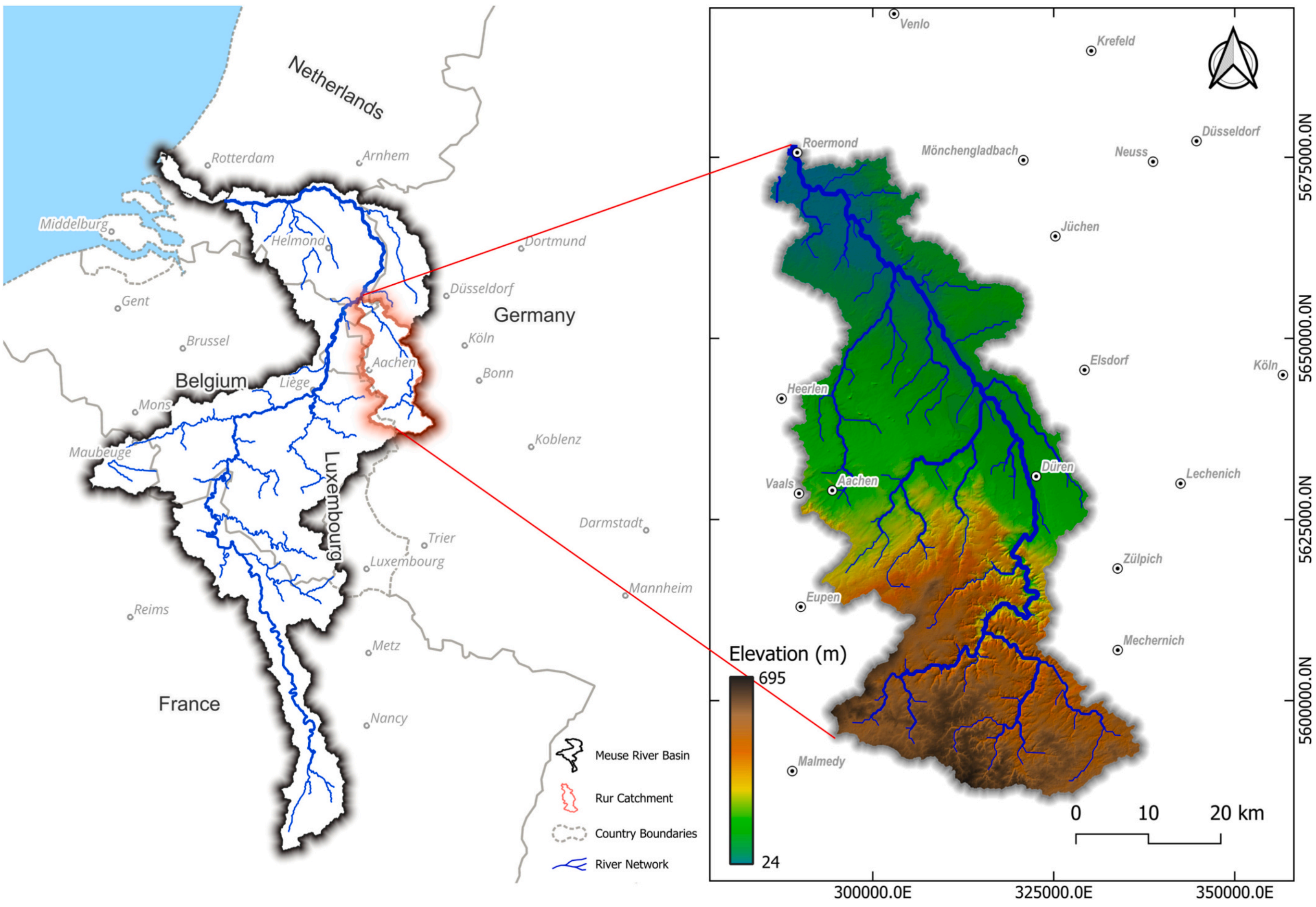

Fig. 1. Map of the study area, Rur catchment. The topography is represented by a digital elevation model (DEM) sourced from the United States Geological Survey (USGS). The catchment boundary and river network are derived from the HydroSHEDS database (Lehner and Grill, 2013; Linke et al., 2019), and country boundaries are sourced from the QGIS World Map vector dataset.

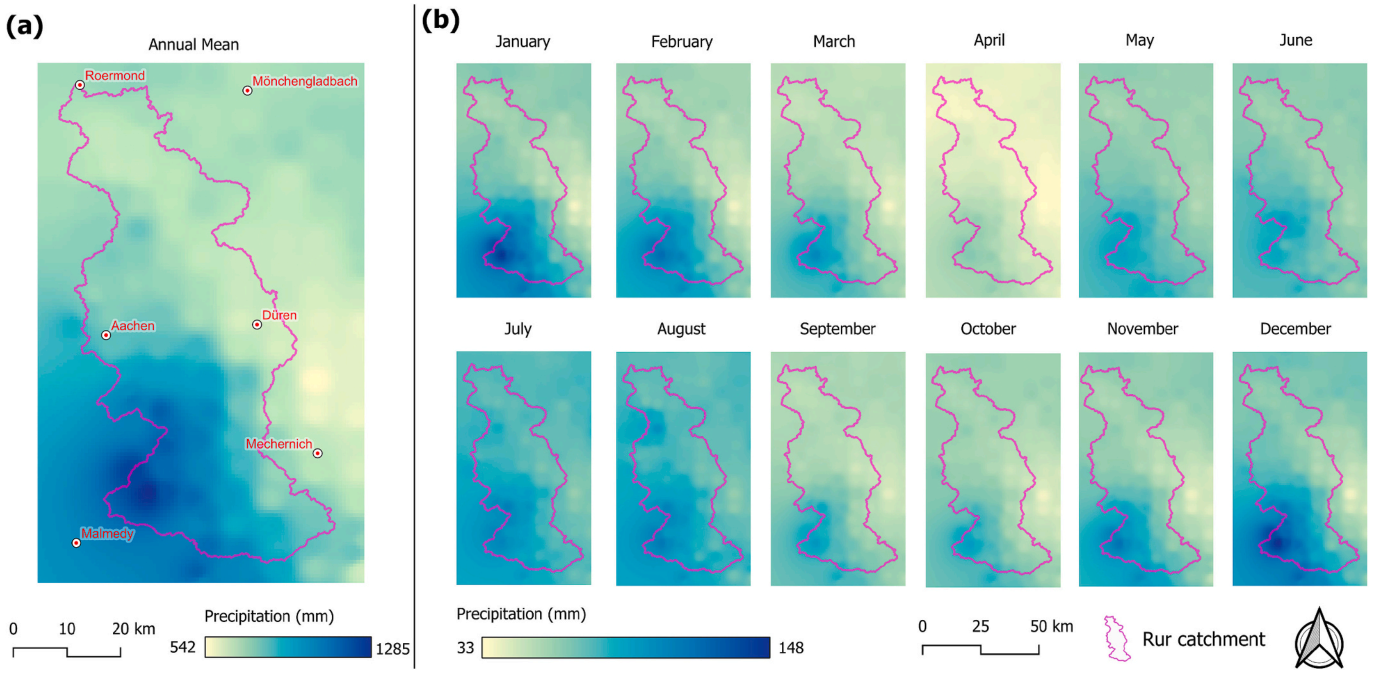

Fig. 2. *Precipitation distribution in the Rur catchment based on monthly observations obtained for the period January 2000 to December 2024: (a) long-term annual mean; (b) long-term monthly mean. Data source: German Weather Service (Deutscher Wetterdienst, 2025b).*

when evapotranspiration is low, whereas in the lowlands summer (April to October) precipitation coincides with higher evaporative demand (Bogena et al., 2005), creating conditions where SM becomes a critical factor for vegetation growth.

Land use and land cover is strongly divided between the northern and southern parts of the catchment (Fig. 3). The northern lowlands form part of the fertile Belgium–Germany loess belt, where arable land dominates with occupying more than one-third of total area and is primarily used for crops such as winter cereals, sugar beet, and maize (Korres et al., 2015; Reichenau et al., 2016). The upland regions are mainly covered by deciduous and coniferous forests (34%) and pastures (22%). Built-up occupies only about 5% of the area, while lignite opencast mining and reservoirs are locally important features (Bogena et al., 2018).

Soils also reflect this north–south division. In the northern loess plains, Haplic Luvisols and Anthrosols with silt loam textures offer high agricultural productivity, with available field capacities exceeding 200 mm. In contrast, the southern upland areas are dominated by Cambisols and Gleysols with lower field capacities ranging from 50 to 150 mm, and in some locations below 30 mm (Bogena et al., 2005).

Hydrologically, the southern bedrock-dominated uplands exhibit flashy runoff and rely on managed reservoirs, while the northern plains contain productive aquifers that support groundwater-dependent ecosystems and water supply (Bogena et al., 2005; Kramm and Hoffmeister, 2020). The catchment has a long history of water stress and competing demands dating to early industrialization, with documented conflicts between agricultural, industrial, and ecological water uses during low-flow periods (Paul, 1994; Wolf et al., 2023b).

Given these characteristics, the Rur catchment represents a heterogeneous landscape where sharp gradients in climate, land use, and soil

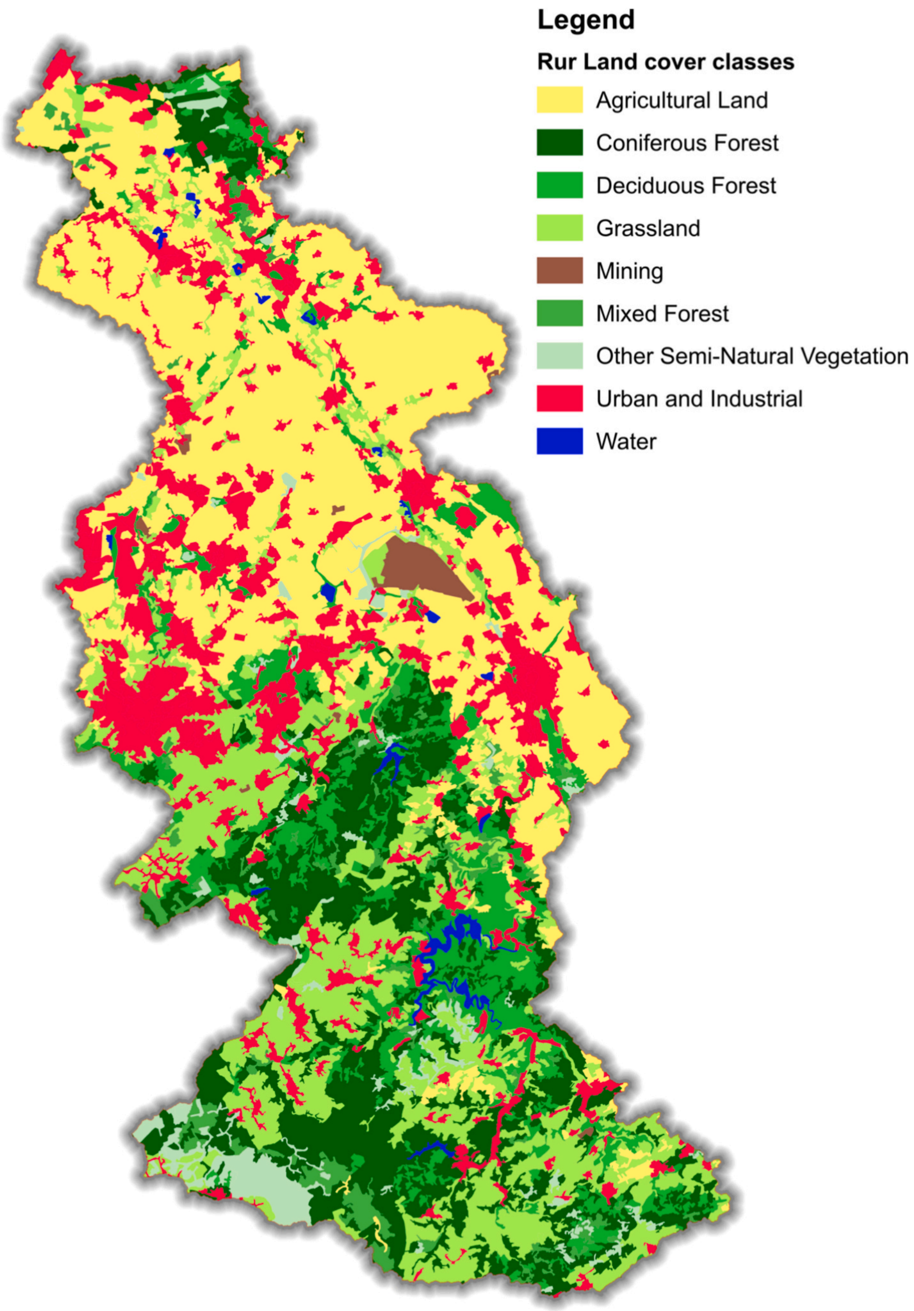

Fig. 3. Land-cover classification map of the Rur catchment. The land cover data is derived from the CORINE Land Cover (CLC2018) inventory (© European Union, Copernicus Land Monitoring Service).

create a natural laboratory for studying SM–vegetation interactions under intermittent water stress. Its well-documented hydroclimatic variability and availability of long-term SM data make the catchment particularly suitable for advancing the understanding of SM–vegetation interactions and their role in agricultural drought assessment.

2.2. Datasets

2.2.1. Soil moisture (SM)

SM data were obtained from the German Weather Service (DWD; Deutscher Wetterdienst, 2025a), where soil water availability is expressed as a percentage of effective field capacity (% nFK; abbreviation for German term of “nutzbare Feldkapazität”). This metric represents the percentage of plant-available water relative to field capacity. Usable field capacity (nFK) is the difference between field capacity and dead water content of the soil, representing the amount of water available to plants (Westerkamp et al., 2024). The effective field capacity (nFK) represents the volume of water stored in the soil that is available to plants. Values below 50% nFK indicate conditions of plant water stress, whereas values above 100% nFK reflect oversaturation. The dataset provides monthly values of gridded SM in 60 cm depth for the entire calendar year for German territories, independent of actual cropping conditions with a resolution of 1 × 1 km. SM is modeled using the Soil–Vegetation–Atmosphere–Transfer (SVAT) model AMBAV, which incorporates the Penman–Monteith equation and is routinely applied in agrometeorological consulting, such as irrigation scheduling (Selzer and Schubert, 2023).

2.2.2. Vegetation dataset (NDVI)

Vegetation conditions were assessed using the MODIS Vegetation Indices product MOD13Q1 (Version 6.1) from the Terra satellite (Didan, 2021). This Level-3 dataset provides the NDVI at a spatial resolution of 250 m and a temporal resolution of 16 days available from 2000 to 02-18 to present. NDVI serves as a widely used proxy for vegetation greenness and productivity, offering continuity with earlier NOAA-AVHRR derived NDVI time series. The MOD13Q1 algorithm selects the best available pixel within each 16-day period, prioritizing observations with minimal cloud contamination, low viewing angle, and maximum NDVI values. In addition to NDVI, the product includes the Enhanced Vegetation Index (EVI), spectral reflectance bands (red, near-infrared, blue, and mid-infrared), and quality assessment layers (e.g., pixel reliability, cloud and aerosol information, and VI quality flags). Version 6.1 incorporates calibration improvements, including corrections for response-versus-scan angle, optical crosstalk, and polarization effects, ensuring higher consistency and accuracy of the vegetation indices. The NDVI from MOD13Q1 product has been extensively validated and used in recent studies investigating drought impacts, phenology, and vegetation-climate interactions (Bogale et al., 2025; Burka et al., 2024; Ghimire et al., 2025; Taheri Qazvini and Carrion, 2023; Zhang et al., 2017).

2.3. Methods

2.3.1. Data preparation and pre-processing

Following data acquisition, SM and vegetation datasets were harmonized to the spatial extent of the Rur catchment and aggregated to monthly and annual scales. Access to DWD SM data is limited to point-based downloads rather than gridded raster formats. To ensure complete catchment coverage, the full set of 2686 observation points was utilized, and monthly SM time series were obtained for the period 2000–2024. For spatial analysis, the point-based SM values were aggregated to annual and long term means and subsequently spatially interpolated using the Inverse Distance Weighting (IDW) method to generate continuous raster layers and spatial distribution maps (Fig. 5).

Meanwhile, the VCI was derived from the MODIS-based NDVI time series using Google Earth Engine (GEE; Gorelick et al., 2017). The MODIS image collection was first filtered for the spatial extent of the Rur catchment, the relevant NDVI band, and the temporal window spanning from 2000 to 2024. Subsequently, the minimum and maximum NDVI values were aggregated, and the VCI was computed. The VCI normalizes NDVI values by relating current vegetation conditions to the historical range for each pixel and is defined as:

$$\mathrm{VCI}_{\mathrm{i,t}} = \frac{\mathrm{NDVI}_{\mathrm{i,t}} - \mathrm{NDVI}_{\mathrm{i}}^{\mathrm{min}}}{\mathrm{NDVI}_{\mathrm{i}}^{\mathrm{max}} - \mathrm{NDVI}_{\mathrm{i}}^{\mathrm{min}}} \times 100 \tag{1}$$

where $NDVI_{i,t}$ is the NDVI value for pixel i at time t, $NDVI_i^{max}$ and $NDVI_i^{min}$ represent the long-term minimum and maximum values at that pixel. This normalization reduces location-specific biases and highlights vegetation stress relative to local potential.

The analysis of vegetation dynamics was restricted to the period from April to September of each year, which represents the principal growing season in the region. This timeframe corresponds to the average phenological presence of active vegetation period on arable land in the Rur catchment, as shown in detailed assessments of vegetation phenology by Waldhoff et al. (2017). Outside this interval, vegetation is largely characterized by bare soil, dormancy in winter, or senescence in late autumn. Evergreen vegetation, such as coniferous forests, maintains greenness throughout the year and can therefore mask crop-related seasonal signals, as the southern hilly parts of the catchment stay green all the year. By focusing on April–September, when agricultural vegetation dominates the landscape, the influence of evergreen cover on the vegetation index dynamics is minimized, ensuring that the derived indices more reliably reflect crop responses to SM variability.

2.3.2. Drought characterization and severity identification

VCI values were extracted from the monthly raster layers at the same point locations where SM data were acquired. To ensure consistency, paired samples were excluded if either SM or VCI data were missing. Drought timing and intensity were first explored through heatmaps of monthly SM and VCI (Fig. 7a, d) across the study period, enabling visualization of drought-affected months and intra-annual variability in vegetation and soil water availability.

Since drought is defined as a relative deviation from local climatic norms rather than by absolute rainfall absence (Wilhite and Glantz, 1985), an objective statistical approach was required. We therefore applied Z-score standardization to both SM and VCI time series (Lee, 1973). This approach is necessitated by the highly localized nature of both SM and the VCI, the requirement to define drought as a relative water deficit within the catchment's specific climatic regime. The Z-score provides a unified metric for quantifying a deficit, regardless of the variable's original unit or distribution. It transforms both SM and VCI into unitless metric, allowing the direct comparison of drought severity based on water stress (SM) and vegetative response (VCI). The Z-score for a given variable X (e.g., SM or VCI) at time t is calculated as:

$$Z_{X,t} = \frac{\mathrm{X_t} - \mu_X}{\sigma_X} \tag{2}$$

where $\mathrm{X_t}$ is the observed value of the variable X in year t, μ_X is the long-term mean of the variable X, and σ_X is the long-term standard deviation of the variable X. Standardization was performed independently for SM and VCI at each time step.

Based on the resulting standardized values, years with $Z > +1$ were classified as wet, years with $Z < -1$ as drought, and values between -1 and $+1$ as normal conditions (Dogan et al., 2012; Gogineni et al., 2025; Noor et al., 2020; Patel et al., 2007). This approach accounts for the localized nature of drought in the Rur catchment and provides a unified framework for comparing SM deficits with vegetation dynamics.

2.3.3. Correlation analysis framework

The statistical relationship between SM and VCI was quantified using Pearson's correlation coefficient (r). This metric assesses the strength and direction of linear coupling between the variables and is a standard approach in time series analysis for identifying limiting factors in mixed-use catchments. The coefficient is calculated as follows:

$$r_{X,y} = \frac{\sum_{i=1}^{n}(x_i - \overline{x})(y_i - \overline{y})}{\sqrt{\sum_{i=1}^{n}(x_i - \overline{x})^2}\sqrt{\sum_{i=1}^{n}(y_i - \overline{y})^2}} \tag{3}$$

where n is the number of data pairs (the length of the vectors X and Y), x_i and y_i are the individual data points, and $\overline{x}$ and $\overline{y}$ are the mean values of the vectors X and Y, respectively. The r ranges from -1 to $+1$, where the values greater than 0 show linear positive correlation of two variables. The higher the coefficient, the stronger the linear correlation between the two variables. The statistical significance of differences in correlation strength was assessed using Kruskal-Wallis test (Kruskal and Wallis, 1952), a non-parametric method for comparing multiple independent groups.

To account for the non-linear and threshold-dependent nature of vegetation response to SM, a two-phase analytical approach was adopted:

- Phase 1: Baseline assessment of SM–VCI relationships using all growing-season observations to characterize the unfiltered, catchment-wide coupling.
- Phase 2: Application of an optimal SM threshold to isolate water-limited conditions, followed by spatial and land-cover-specific re-evaluation of SM–VCI correlations to reveal the clarified drought signal.

2.3.3.1. Baseline (unfiltered) correlation analysis. First, Pearson correlations were computed using all available paired SM–VCI observations from April–September (2000–2024) to establish a catchment-wide baseline. This included:

- Pooled seasonal correlation – all monthly data aggregated across the catchment (Fig. 8a).
- Monthly correlations – computed separately for each growing-season month (Fig. 8b).

These baseline results quantify the inherent noise and weak coupling when non-water-limited periods are included.

2.3.3.2. Optimal SM threshold determination. To isolate periods when vegetation is water-limited and to reduce noise associated with SM saturation, we implemented a data-driven threshold optimization procedure. This approach is grounded in the ecological principle that vegetation responds nonlinearly to SM, with strong coupling occurring primarily under water-limited conditions (Fu et al., 2022b; Li et al., 2023; Seneviratne et al., 2010; Teuling et al., 2006).

We systematically tested upper thresholds defined by percentiles p of the SM distribution (from 10th to 90th percentile in 5% increments). For each candidate threshold T_p, data with SM values above the cutoff were excluded, and the correlation was recalculated on the remaining subset.

Threshold is expressed mathematically as follows:

$$T_p = Q_{SM}\left(\frac{p}{100}\right) \tag{4}$$

where $Q_{SM}(q)$ is the q-th quantile of the SM distribution. For each threshold, a filtered dataset D_p was created:

$$D_p = \{(x_i, y_i) \in D \mid x_i \le T_p\} \tag{5}$$

where x_i represents SM and y_i represents VCI for observation i, and D is the complete dataset. The Pearson correlation $r_p = cor(D_p)$ is then computed using eq. 3, and the optimal threshold T_{opt} was then selected as the threshold yielding the maximum correlation coefficient:

$$T_{Opt} = \{T_p \mid r_p = \max(r_{10}, r_{20}, \ldots, r_{90})\} \tag{6}$$

T_{Opt} represents the transition from energy-limited to water-limited land-atmosphere exchange regimes (Fig. 9). This threshold defines the dataset for all subsequent analyses, ensuring that the identified relationships reflect conditions where SM is a limiting factor for vegetation health.

To assess the temporal stability of the optimal SM threshold, we employed a leave-one-out (LOO) cross-validation approach (Roberts et al., 2017; Stone, 1974). This approach tests whether the threshold identified from the full dataset remains robust when individual years are systematically withheld, thereby assessing its generalizability across different temporal subsets.

2.3.3.3. Correlation analysis under water-limited conditions. To capture both catchment-scale patterns and local heterogeneity in the SM–VCI relationship, correlations were examined at two complementary levels using only data where SM ≤ optimal threshold:

- **Geospatial correlation mapping:** Pearson correlations were calculated for each monitoring point (pixel grid) using monthly filtered data. Correlations were computed only for location-months with a minimum temporal coverage of 20%, up to a complete set of available observations for the full 25-year period. This threshold ensured statistical reliability while maximizing spatial coverage to detect catchment-wide drought sensitivity patterns. Resulting coefficients were interpolated via IDW to produce continuous correlation maps (Fig. 10).
- **Land-cover-specific correlation:** To evaluate the influence of land cover type on the SM–VCI relationship, a land-cover-mediated correlation analysis was performed, which is an essential step to move beyond spatial mapping. The Corine Land Cover (CLC) inventory for the Rur catchment was acquired and reclassified into 9 different classes (Fig. 3). Non-vegetated areas (e.g., urban/industrial, water bodies, and mining areas) were excluded from this analysis to focus on vegetation-oriented SM–VCI interactions. For months in which a meaningful SM–VCI relationship was detected under the water-limited regime (i.e., months with valid correlations after threshold filtering), correlation distributions were summarized and visualized via grouped boxplots (Fig. 10).

The overall methodological workflow is illustrated in Fig. 4.

3. Results

3.1. Spatiotemporal patterns of SM

The long-term annual mean SM (% nFK) across the 2000–2024 period (Fig. 5a) reveals a pronounced south–north gradient in mean soil water availability across the Rur catchment. The southern uplands exhibit the highest mean SM values (≈ 86–93% nFK), whereas the northern lowlands maintain comparatively lower averages (≈ 83–86% nFK). These spatial patterns suggest the combined influence of topography variation, precipitation distribution, and land cover.

Interannual variations in SM (Fig. 5b) highlight several distinct relatively dry years with catchment-wide annual mean SM below 80% nFK, notably 2003, 2011, 2018, 2020, and 2022. Earlier periods of SM deficit are evident, notably around 2003 and to a lesser extent in 2011, although these appear less spatially extensive and persistent than the recent 2018–2022 dry years.

The southern region, despite having higher mean SM, still experienced relatively low moisture values during peak dry years. In contrast, the northern catchment exhibited a magnified response, falling into extreme SM deficit during these periods.

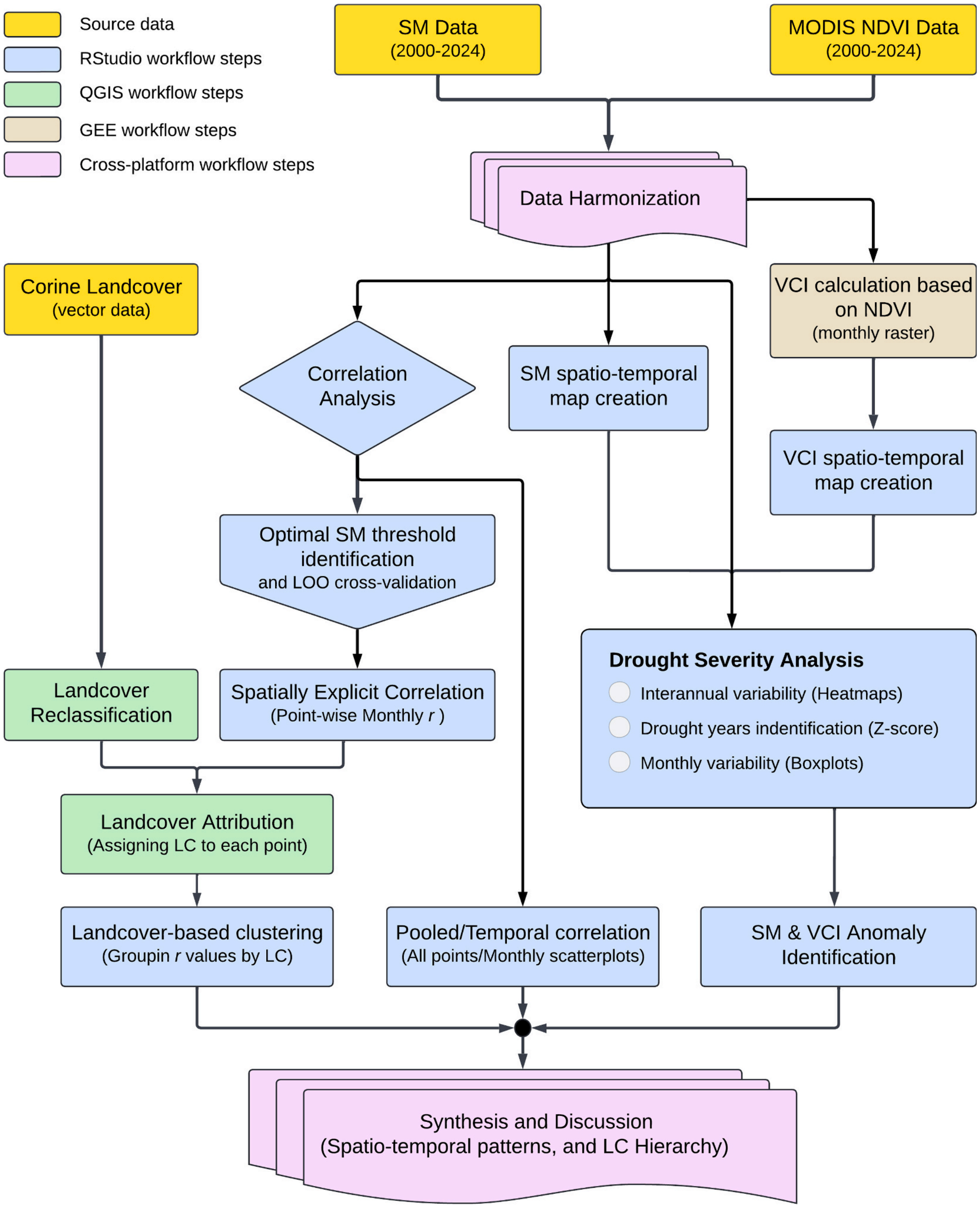

Fig. 4. Methodological workflow for analyzing spatiotemporal drought severity, SM–VCI coupling analysis and its land cover controls in the Rur catchment.

3.2. *Spatiotemporal patterns of vegetation stress*

The annual mean VCI maps (Fig. 6) illustrate spatiotemporal variability in vegetation conditions across the Rur catchment during the period of 2000 to 2024. Forested upland areas in southern part of the catchment, show consistently high VCI values (≈ 80–100, bright green) throughout the period, indicating stable vegetation greenness and low interannual variability. In contrast, the agricultural lowlands, the northern and central parts, display pronounced interannual fluctuations in VCI values (≈ 50–60, yellow/orange), especially during relatively dry years such as 2001, 2003, 2006, 2018, 2020, and 2022. These years are characterized by widespread reductions in VCI, while wetter years (e.g., 2002, 2005, 2009, 2016, 2023) exhibit greenness and higher VCI values. A distinct cluster of persistently low VCI values appears in the northeastern lowlands of the catchment, clearly visible as localized red patches in the long-term VCI composite. These areas correspond to the lignite mining zone, where large-scale excavation, soil removal, and vegetation disturbance produce a consistently degraded spectral signal. As a result, the low VCI values observed in this region do not reflect drought-driven vegetation stress but are instead a consequence of permanent land cover alteration associated with mining activity.

3.3. *Drought characterization and severity identification*

To characterize drought patterns and objectively identify severe episodes, we first visualized the monthly spatiotemporal variability of SM and VCI via heatmaps and boxplots. We then computed *Z*-scores for both variables (2000–2024) to quantify drought severity (Fig. 7), defining drought years as those with $Z < -1.0$ (Dogan et al., 2012; Gogineni et al., 2025; Patel et al., 2007).

SM anomalies: The heatmap reveals recurrent, multi-month SM deficits which mostly start in April and persist until September,

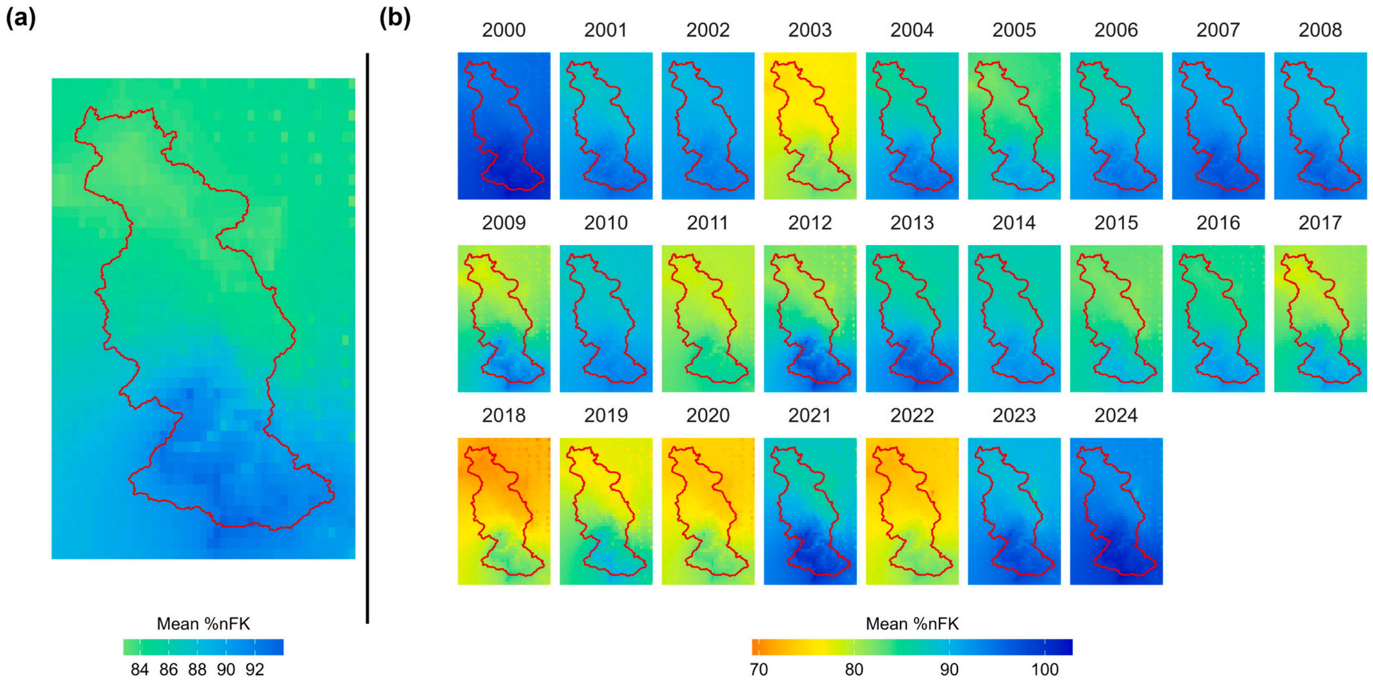

Fig. 5. Spatial patterns of SM (% nFK) in the Rur catchment: (a) long-term mean (2000–2024) and (b) interannual mean values. Data source (Deutscher Wetterdienst, 2025a).

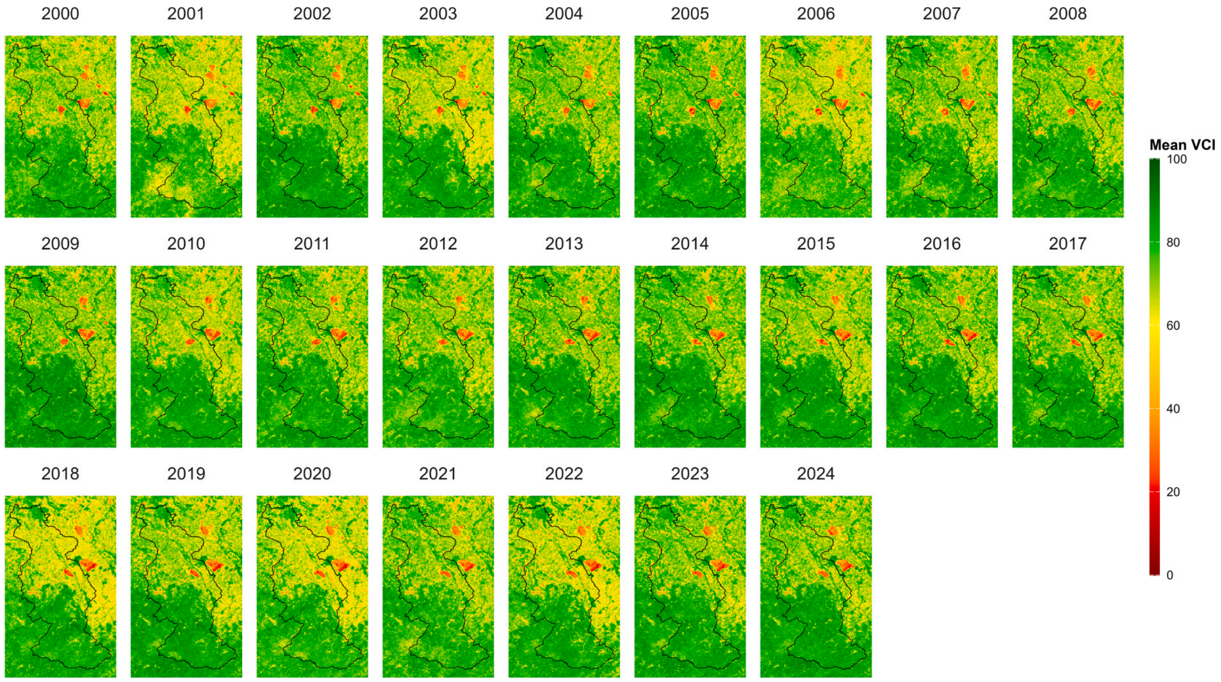

Fig. 6. Spatial distribution of the annual mean VCI across the Rur catchment, derived from MODIS-based NDVI observations.

confirming the agricultural period (Fig. 7a). The Z-score reveals recurrent annual mean SM deficits in the years 2003, 2018, 2020, and 2022; however, 2011 and 2019 remain marginally above the -1 drought threshold (Fig. 7b). These periods correspond to widespread and prolonged reductions in soil water availability. The monthly SM boxplots (Fig. 7c) indicate strong seasonal variability, with the lowest medians and highest interquartile ranges between June and September. During this period, the catchment experiences maximum evaporative demand, confirming late summer as the peak dry season. Conversely, the winter and early spring months display near-saturated conditions (median $\approx$ 100% nFK) with minimal variability, reflecting recharge-dominated periods.

Vegetation anomalies: The VCI heatmap represents the monthly vegetation dynamics, clearly distinguishing months with stressed and healthy vegetation (Fig. 7d). The Z-score graph which is calculated based on the VCI values from growing season (April – September), exhibits similar interannual drought patterns, with the most pronounced vegetation deficits ($Z < -1$) occurring during 2001, 2003, 2006, 2018, 2020, and 2022 (Fig. 7e). Monthly VCI boxplots (Fig. 7f) further reveal the seasonal evolution of vegetation greenness, with the lowest values

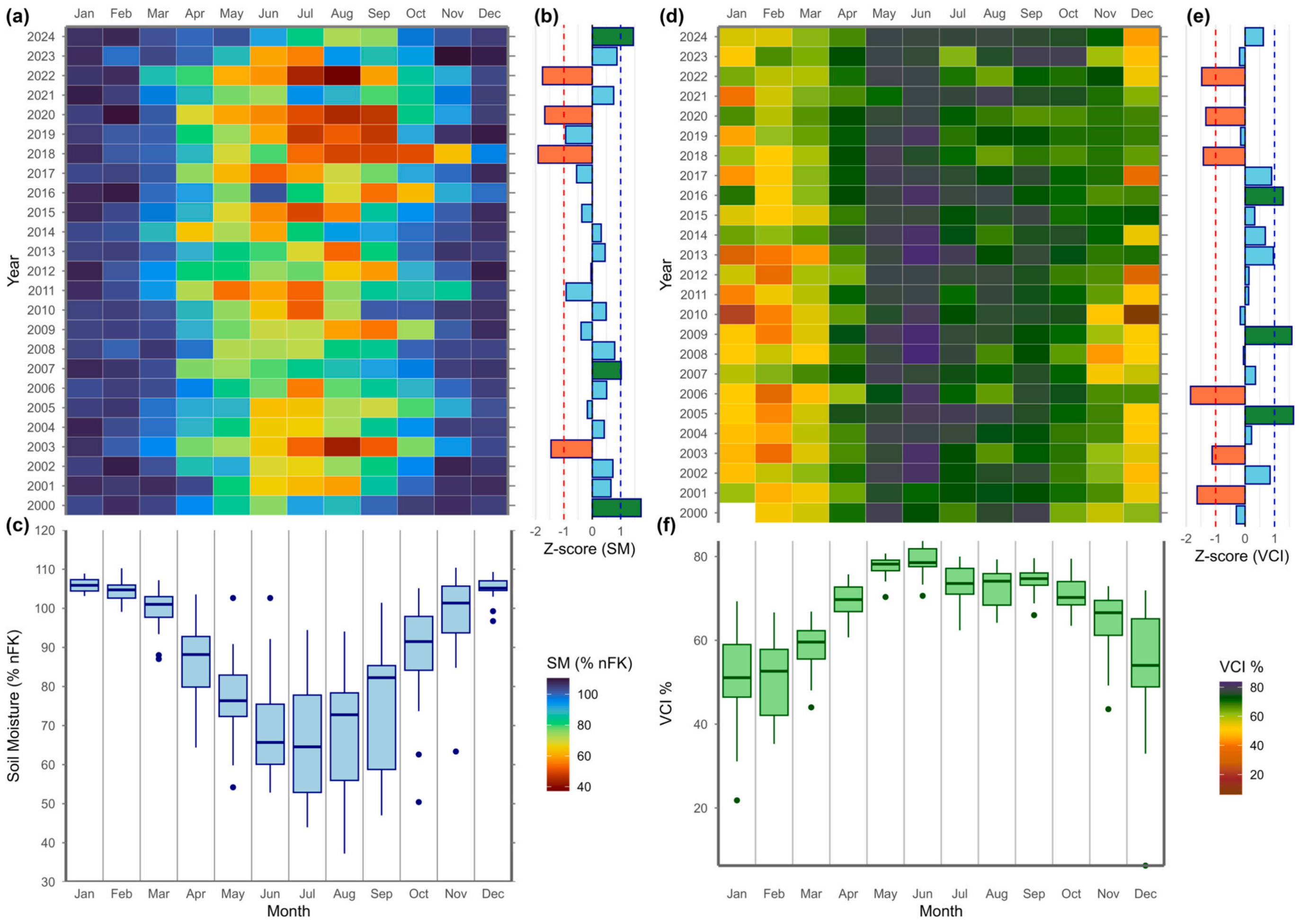

Fig. 7. Drought severity analysis of SM and vegetation stress in the Rur catchment: (a) heatmap of monthly SM, (b) SM Z-scores, (c) monthly boxplots of SM, (d) heatmap of monthly VCI, (e) VCI Z-scores, and (f) monthly boxplots of VCI. Data sources: SM from (Deutscher Wetterdienst, 2025a); VCI from MODIS NDVI (MOD13Q1), processed in GEE.

occurring in the winter months (October to March). In the growing season starting from April (median ≈ 67.5), corresponding to early vegetative development, VCI increases and reaches its peak in May–June (median ≈ 77.5). Thereafter, values gradually decline, reflecting crop harvesting and increasing soil water stress during late summer.

3.4. Heterogeneous coupling of SM and VCI

To quantify the strength and spatial variability of SM–VCI interactions, Pearson correlation coefficients were computed following a two-phase approach: baseline assessment with all data, followed by refined analysis under water-limited conditions.

3.4.1. Catchment-wide pooled correlation (baseline)

Pooling all SM and VCI observations from April to September across the catchment reveals a weak but statistically significant correlation ($r = 0.109$, $p < 0.001$; Fig. 8a). To examine this temporal evolution in greater detail, monthly pooled scatterplots were generated revealing a distinct temporal evolution of the coupling strength and confirming a shift in the primary limiting factor across the growing season (Fig. 8b). The monthly pooled analyses reveal a progressive strengthening of the SM–VCI coupling through the growing season, however still with weak correlation. Correlations are near zero or slightly negative in April ($r = -0.07$), but from May onward, the values increase steadily, reaching a maximum in September ($r = 0.27$). While the pooled analysis clearly captures this temporal progression, the low maximum correlation ($r = 0.27$) highlights that the true strength of the SM–VCI relationship emerges only under water-limited conditions, necessitating spatially explicit and land cover-stratified analyses after regime separation.

3.4.2. Identification of optimal SM threshold

To isolate periods when SM actively limits vegetation, we implemented a data-driven threshold optimization procedure. The baseline Pearson correlation between SM and the VCI across all growing-season observations (April–September 2000–2024) was weak, ($r = 0.109$), indicating minimal direct relationship under non-stress conditions (Fig. 8a).

Systematic threshold testing from the 10th to 90th percentile of SM values revealed a distinct optimal threshold at SM ≤ 64% nFK, where the SM–VCI correlation peaked at $r = 0.354$ with $p < 0.001$ (Fig. 9a). This represents a 225% relative increase in correlation strength compared to the baseline ($r = 0.109$), corresponding to an increase in explained variance (r^2) from 1.2% to 12.5%, approximately a tenfold gain in the proportion of vegetation variability explained by SM. A broad plateau of high correlation (61–64% nFK) was observed in the full dataset, where all thresholds yield $r > 0.34$.

To assess the robustness of this relationship to potential nonlinearity, we also computed Spearman's rank correlation (ρ) across all tested thresholds (Fig. A1). The Spearman values closely tracked the Pearson results throughout. The optimal threshold for Spearman was 61% nFK, with a correlation coefficient of $\rho = 0.359$. The application of this threshold retained 30.3% (122,469 observations) of the original data

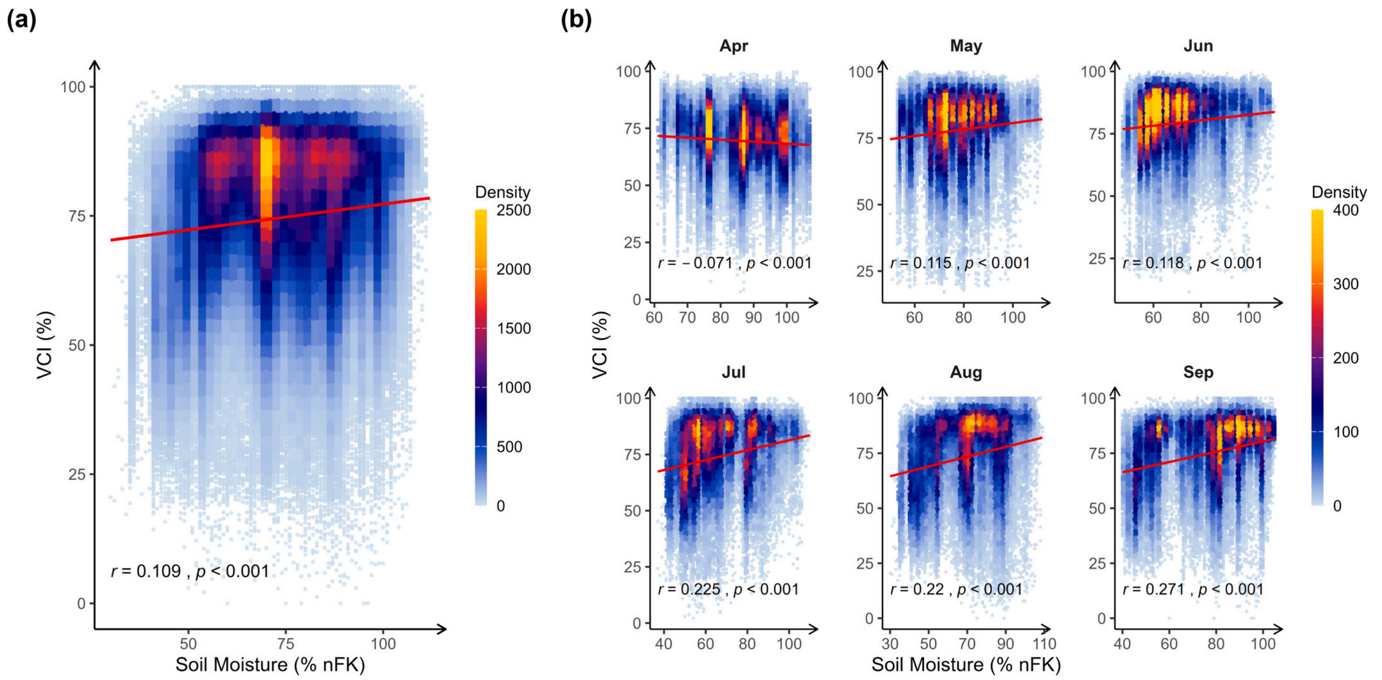

Fig. 8. Baseline and monthly relationships between SM and VCI during the growing season for the Rur catchment from 2000 to 2024, (a) Baseline correlation between monthly SM and VCI (all months pooled), and (b) Monthly SM–VCI relationships (April–September). Data sources: SM from (Deutscher Wetterdienst, 2025a); VCI from MODIS NDVI (MOD13Q1), processed in GEE.

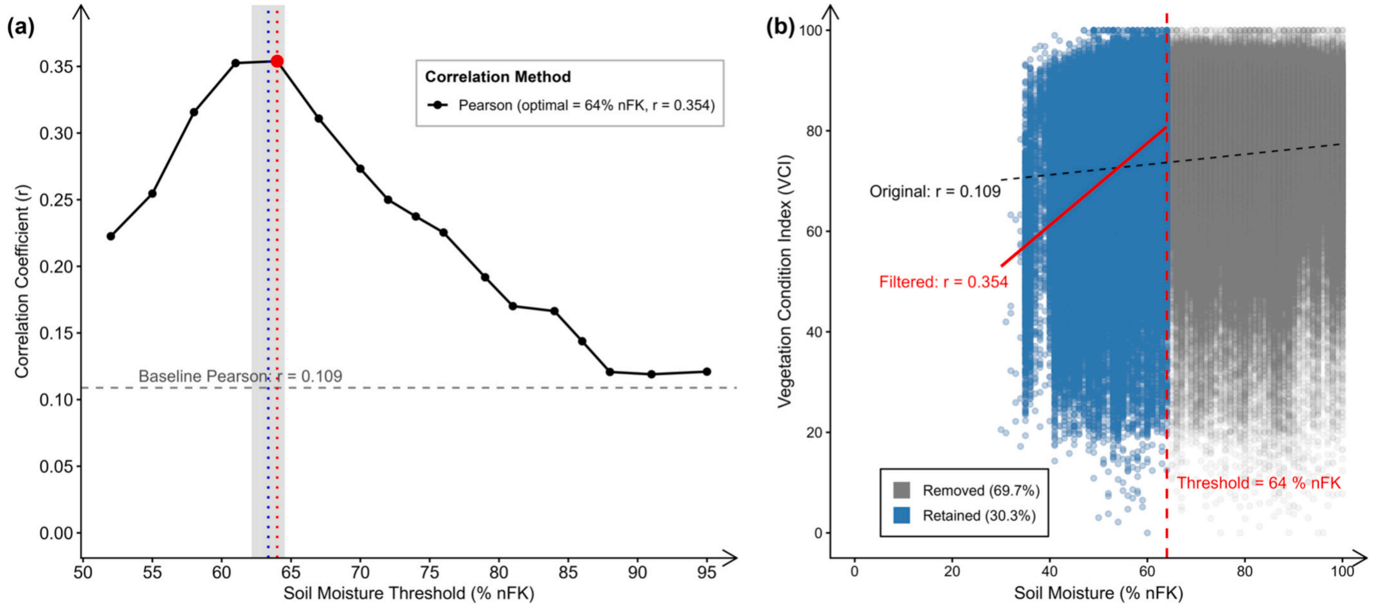

Fig. 9. SM threshold optimization for detecting drought-stress impacts on vegetation. (a) Pearson correlation coefficient (r) between SM and VCI as a function of SM threshold. The red point indicates the optimal threshold (64% nFK, r = 0.354). The gray envelope shows ±1.6 standard deviation around the LOO cross-validation mean threshold (63.6 ± 1.6% nFK). (b) Percentage of observations retained (30.3%) and removed (69.7%) by applying the optimal threshold. Data sources: SM from (Deutscher Wetterdienst, 2025a); VCI from MODIS NDVI (MOD13Q1), processed in GEE. (For interpretation of the references to colour in this figure legend, the reader is referred to the web version of this article.)

points, providing a robust filtered dataset for subsequent drought-stress analysis while filtering out 69.7% of observations that occurred under non-water-limited conditions (Fig. 9b).

To assess the temporal stability of the identified 64% nFK threshold, we performed a LOO cross-validation across the 25-year study period (2000–2024). In each iteration, one complete year was excluded from the dataset, and the optimal threshold was determined using the remaining 24 years. The optimal threshold showed remarkable stability, with a mean of 63.6% nFK (±1.6% SD) across all iterations and correlations consistently ranging from 0.332 to 0.371, with 92% of iterations (23 out of 25 years) falling within one standard deviation of the mean (62.1–65.2% nFK; Fig. 9a, gray envelope). The 64% threshold was selected most frequently (9 years, 36% of years), confirming its robustness and ecological relevance (see Appendix A Table A1 and Fig. A2 for full LOO cross-validation results). Notably, the LOO cross-validation envelope (62.1–65.2% nFK) falls largely within the broad plateau of high correlation (61–64% nFK) observed in the full dataset.

3.4.3. Spatial patterns of correlation

Applying the optimal SM threshold (SM $\leq$ 64% nFK) substantially altered the spatiotemporal coverage of valid SM–VCI correlations across the catchment. After filtering, April yielded no valid correlation points because SM values consistently exceeded the threshold; May retained only 66 points (2.5% of the catchment), whereas June included 2543 points (95% of the catchment), with the remaining 5% of the area interpolated based on the available observations. The months of July, August, and September retained complete coverage of 2686 points (100%), confirming that late-growing-season conditions are predominantly water-limited across the entire study area. The spatial evolution of the SM–VCI relationship under these water-limited conditions is depicted in Fig. 10.

In May, the few valid correlations located in the northern lowlands show weak positive relationships (r = 0.25), suggesting early but localized water stress in predominantly agricultural areas. Furthermore, June exhibits the lowest mean correlation (r = 0.046) despite near-complete spatial coverage. During this month, much of the southern forested uplands show weak or slightly negative correlations, indicating continued decoupling from surface SM.

A marked shift occurs in July, where correlations strengthen noticeably (mean r = 0.215) and positive coupling expands spatially. The northern agricultural zone begins to show relatively higher correlations than the southern part. The strongest and most extensive coupling occurs in August, which shows the relatively highest mean correlation (r = 0.501) and the most spatially homogeneous positive pattern. Nearly the entire catchment exhibits moderate to strong positive correlations, with the agricultural lowlands reaching (r > 0.7) in many parts. This peak reflects the convergence of high atmospheric water demand and declining SM reserves during the warmest month of the growing season.

By September, coupling strength declines (mean r = 0.213) but remains positive across most of the catchment. The spatial pattern resembles July but with slightly weaker correlations in the northern part, suggesting reduced water stress as temperatures decline and evaporative demand lessens. Additionally, harvesting of summer crops in the central and northern parts of the catchment during this period removes actively transpiring vegetation, further decoupling surface SM from VCI signal. The corresponding statistical summary for each month is presented in Fig. 11.

3.4.4. Land-cover-based clustering of SM–VCI correlation

A clear hierarchy in SM–VCI coupling strength emerged when correlations were stratified by land cover type under water-limited conditions (Fig. 12). Across all vegetated classes, correlation strength followed a consistent seasonal trajectory, increasing from May through July, peaking sharply in August, and declining slightly in September.

Agricultural land and grassland exhibited the strongest positive coupling among others throughout the growing season. For example, for grassland, median correlation coefficients increased from approximately $r \approx 0.3$ in May to peak values exceeding $r = 0.75$ in August, before declining in September. In contrast, all forest types (deciduous, mixed, and coniferous) showed markedly weaker coupling, with median correlations generally remaining below $r = 0.2$ and frequently close to zero across all months.

Temporally, correlation strength across all land cover classes closely tracked the seasonal progression of water limitation, confirming August as the period of peak moisture–vegetation coupling and maximum drought sensitivity within the catchment.

4. Discussion

This study provides a multi-faceted analysis of the SM–vegetation relationship in the Rur catchment, integrating long-term spatiotemporal patterns, agricultural drought severity quantification, and a detailed investigation of the SM–VCI coupling after optimal SM threshold selection. Our findings collectively demonstrate that the linkage between soil water availability and vegetation health is not a simple, universal relationship but is instead strongly mediated by seasonality, spatial heterogeneity, and land cover type.

4.1. Spatiotemporal patterns of SM and VCI

Our results confirm a persistent south-north gradient in mean SM (Fig. 5a), a pattern likely driven by higher precipitation in the southern uplands (Fig. 2), and variations in soil types across the catchment. However, the interannual analysis reveals that this generally wetter southern region is not immune to drought, as evidenced by the significant drying during periods like 2003, 2018–2020 and 2022 (Fig. 5b). This establishes that low precipitation translates into catchment-wide SM deficits, albeit with varying intensity.

The vegetation response, captured by VCI, mirrors this spatiotemporal complexity but adds a critical layer of land cover dependency. The consistently high VCI in the forested south (Fig. 6), even during known dry years, indicates a high level of vegetation resilience, likely supported by deeper root systems that access subsurface water stores. Additionally, previous studies have demonstrated that well-developed forest canopies can enhance SM by reducing surface temperatures and limiting soil evaporation (Hasselquist et al., 2018; Royer et al., 2012; Wei et al., 2022; Zuo et al., 2024). In contrast, the agricultural lowlands in the north and central catchment exhibit high interannual variability, with VCI sharply declining during drought years. This aligns with the lower baseline SM in this region and reveals their role as the catchment's primary drought-vulnerable hotspot.

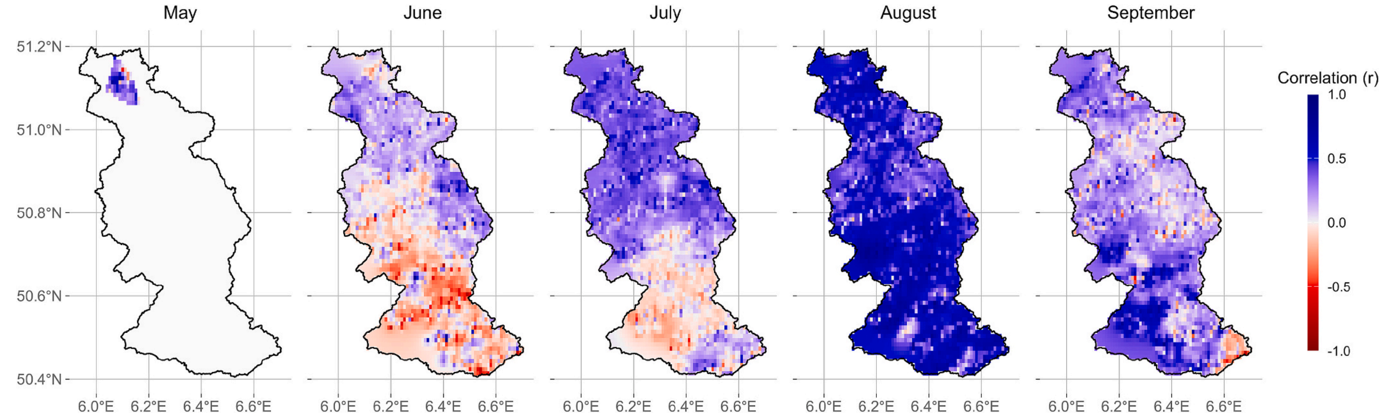

Fig. 10. Spatial distribution of monthly Pearson correlation coefficients between SM and VCI across the Rur catchment.

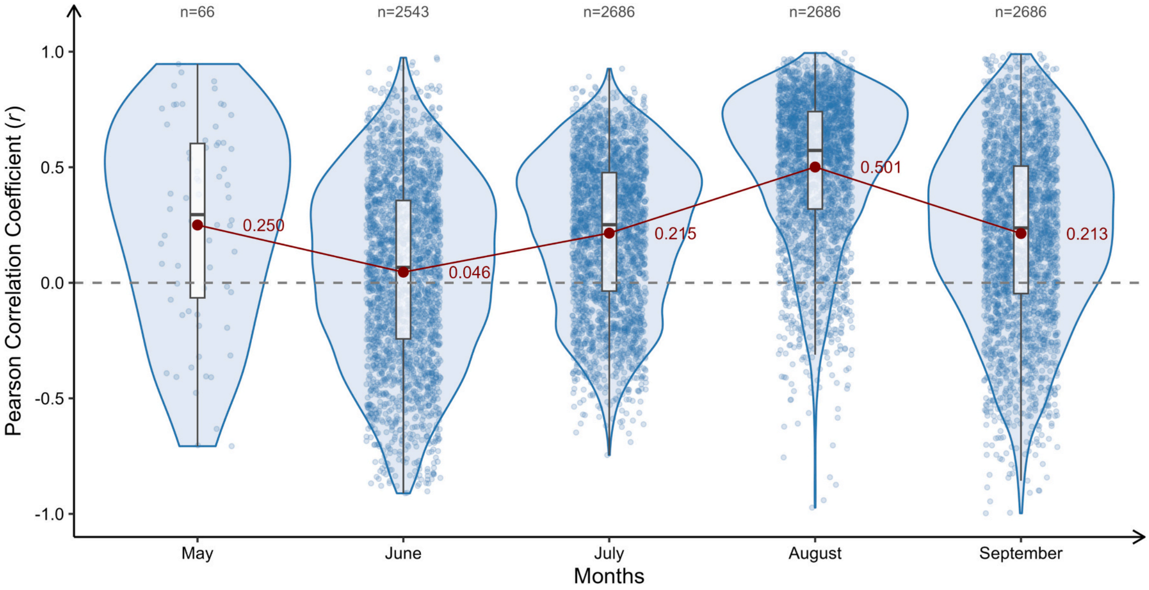

Fig. 11. Monthly distribution of SM–VCI coupling strength (r) for moisture-limited observations (SM $\leq$ 64% nFK).

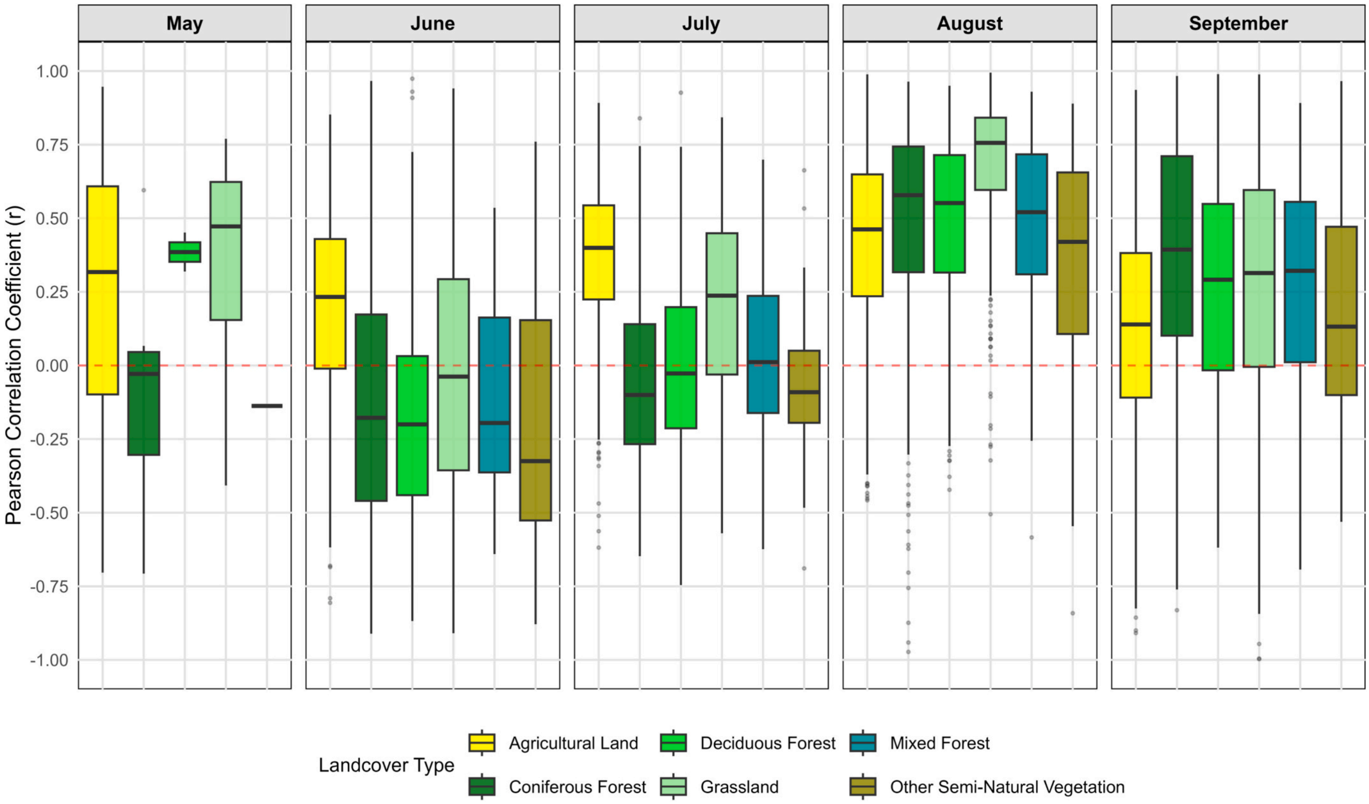

Fig. 12. Distribution of Pearson correlation (r) between SM and VCI grouped by six major vegetated land cover type for the months of July, August, September, and their Seasonal Mean.

The drought characterization (Fig. 7), specifically the *Z*-score analysis (Fig. 7b, e) effectively synthesizes these patterns, objectively identifying major drought years (e.g., 2003, 2018, 2020, 2022) and confirming the synchrony between SM deficits and vegetation stress. However, divergences in 2001 and 2006, where VCI indicates drought conditions but SM appears normal, suggest vegetation stress driven by factors beyond SM deficits. To corroborate this interpretation, we examined temperature anomalies from ERA5-Land reanalysis data (Muñoz Sabater, 2019) (See Appendix B, Fig. A3). In 2001, April temperatures were 2.04 °C below the long-term mean (Fig. A3b), confirming that the observed VCI stress reflects phenology-driven stress—spring cold conditions delayed green-up independently of SM availability. In 2006, July temperatures were 3.91 °C above the mean, coinciding with the well-known severe European heatwave (Rebetez et al., 2009; Struzewska and Kaminski, 2008). This extreme heat likely caused high vapor pressure deficits, leading to stomatal closure independent of SM conditions. In contrast, the coupled drought years (2003, 2018, 2020, 2022) all exhibited positive summer temperature anomalies (ranging from +1.2 °C to +2.5 °C; Table A2), consistent with atmosphere-driven stress where high temperatures exacerbate water demand. These discrepancies underscore the complexity of drought impacts on vegetation, where atmospheric conditions (e.g., thermal limitations in 2001 versus atmospheric aridity in 2006) can decouple vegetation response from soil water availability. The overall synchronization between SM and VCI during extreme drought years is a prerequisite for a meaningful SM–VCI coupling, which we investigated in section (3.4). Importantly the recurrence of these specific drought episodes aligns with established hydroclimatic records for Germany and Central Europe (Gessner et al., 2023; Rukh et al., 2023; Sodoge et al., 2024; Wang et al., 2025), thereby validating our methodological approach and situating our catchment-specific findings within the broader regional climate context of increasing drought frequency and intensity.

4.2. *The SM–VCI coupling*

The evolution of SM-VCI coupling, from a weak catchment-wide pooled relationship to a distinct, threshold-based characterization of water-limited conditions, fundamentally reshapes our understanding of drought sensitivity in the Rur catchment. The initial pooled correlation was statistically significant but weak ($r = 0.109$, $p < 0.001$; Fig. 8a)—a common result in humid-region studies where water limitation is intermittent and multiple ecological factors collectively influence vegetation dynamics (Meng et al., 2022). The monthly progression from near-zero in April to a maximum of $r = 0.27$ in September confirms that coupling is seasonally dependent, strengthening as atmospheric demand increases and SM reserves decline (Fig. 8b).

However, a meaningful interpretation of the SM–VCI relationship in humid systems requires first isolating periods of genuine water limitation. This approach is grounded in land-atmosphere coupling theory which posits that ecosystems operates in distinct energy-limited or water-limited regimes depending on SM availability (Seneviratne et al., 2010; Teuling et al., 2006). While previous work has documented regime transitions through atmospheric and flux-based proxies—capturing the forcing side of land-atmosphere coupling—our study focuses on the response side: vegetation health itself. This distinction is critical for agricultural drought assessment, where the primary concern is not how dry the soil is, but whether that dryness translates into measurable vegetation stress.

To operationalize this theoretical framework, we introduced a data-driven SM threshold to isolate water-limited conditions. By systematically testing correlation strength across SM percentiles, we identified SM $\leq$ 64% nFK as the critical transition point below which SM becomes a primary limiting factor for vegetation health conditions. The empirical results validate this theoretical construct. Filtering the dataset to observations below this threshold increased the catchment-wide SM–VCI correlation from $r = 0.109$ to $r = 0.354$, representing a 225% improvement in correlation strength. In terms of explained variance, this corresponds to an increase in r^2 from 1.2% to 12.5%, indicating an approximately tenfold increase in the proportion of vegetation variability explained by SM.

The robustness of the threshold is supported by its consistency across correlation metrics. Spearman's rank correlation, which is less sensitive to nonlinearity and outliers, identified a slightly lower optimal threshold (61% nFK, $\rho = 0.359$). However, both values lie within a plateau of high correlation (61–64% nFK; $r/\rho > 0.34$; Fig. A1). The 64% threshold was selected as the operational value because it provides a more conservative early-warning benchmark while remaining within the range of high predictive skill. The close agreement between Pearson and Spearman, particularly near the peak, indicates that the SM–VCI relationship under water-limited conditions is approximately linear and monotonic, and that the threshold choice is not dependent on the statistical method. Spearman's rank correlation is also less sensitive to the influence of extreme drought months, further confirming that our results are not driven by a few anomalous years or uneven variance in the data.

Together, these results demonstrate that regime separation—a theoretical concept—has tangible consequences for vegetation response and can be detected through vegetation-defined thresholds. The theoretical and empirical insights carry practical implications. Our empirically derived threshold of 64% nFK provides a catchment-specific refinement of the general 50% nFK agronomic guideline for whole Germany, suggesting that generic thresholds may underestimate drought sensitivity in certain landscapes. The higher value likely reflects the integrated response of the catchment's vegetation mosaic to SM declines, which begin to exhibit stress before classical SM depletion thresholds are reached, making it more sensitive for early warning while remaining ecologically grounded.

This threshold corresponds to only 30.3% of growing-season observations representing water-limited conditions, underscoring that surface SM is a meaningful drought indicator only during a relatively narrow but critical window. During most of the growing season (SM > 64% nFK), vegetation is not water-limited, and other factors—such as temperature, radiation, or management practices—dominate productivity (Jiao et al., 2021), explaining the noise typical of unfiltered analyses.

The temporal evolution of SM–VCI coupling under this threshold reveals a dynamic “coupling curtain” that expands seasonally across the catchment (Figs. 10 and 11). In April, SM remains above the threshold catchment-wide, yielding no valid correlations. By May, only 2.5% of the area—confined to the northern agricultural lowlands—shows sensitivity, marking these zones as first responders to emerging water stress. This area expands to 95% in June and reaches complete catchment-wide coverage (100%) from July through September. This progression illustrates a “drying front” that moves from lowlands to uplands, eventually locking the entire landscape into moisture dependency by peak summer.

Spatially, coupling patterns under water-limited conditions reveal a fundamental dichotomy between the northern-central agricultural lowlands and the southern forested highlands, governed by rooting depth and land use (Fig. 10 & Fig. 12). This pattern is clearly explained by land-cover stratification: agricultural land and grassland showed the strongest coupling, with median correlations exceeding $r = 0.75$ in August, while all forest types exhibited persistently weak correlations (median $r < 0.2$). This hierarchy directly reflects differences in plant-water access: shallow-rooted crops are tightly coupled to surface SM, whereas forests tap deeper water sources and employ multiple strategies to buffer short-term surface drying. These strategies include regulating water use by prioritizing stem rehydration over carbon assimilation during drought (Peters et al., 2023), rapidly recovering from small rainfall events through foliar and root water uptake while benefiting from reduced atmospheric demand (Dietrich and Kahmen, 2019), and flexibly shifting water uptake between soil layers—accessing fresh precipitation from topsoil within days while relying on seasonally stored water from deeper layers during prolonged dry periods (Kinzinger et al., 2025). Temporally, coupling strength peaks in August (mean $r = 0.501$), when high evaporative demand overrides even the buffering capacity of forest root systems, leading to catchment-wide synchronization in water stress. By September, coupling weakens asymmetrically: agricultural areas decouple earlier, likely due to crop harvesting, while forests remain coupled as perennial vegetation continues to track SM availability. This land-cover-dependent decoupling timing illustrates how vegetation functional type modulates seasonal drought vulnerability.

In conclusion, our two-step filtering approach—seasonal selection to ensure vegetation is active, followed by a SM threshold to exclude non-limiting wet conditions—addresses a fundamental divergence in SM–vegetation coupling between arid and humid regions. In arid systems, vegetation is perennially water-limited, making SM a reliable indicator throughout the growing season (Li and Sawada, 2022; L. Liu et al., 2020; Wei et al., 2022; Yang et al., 2023). In contrast, humid temperate systems like the Rur catchment, experience alternating periods of water sufficiency and limitation (Wolf et al., 2023a; Wolf et al., 2023b). Our method isolates the critical, narrow window within the growing season when SM transitions from a non-limiting to a limiting factor, thereby resolving the signal noise that has long complicated SM–VCI studies in such regions. This threshold-driven framework shifts the paradigm for humid-region drought monitoring. Rather than seeking a universal SM–VCI relationship—an approach more suited to arid climates—effective monitoring must track the progression of the "coupling curtain" to identify when and where the landscape becomes water-limited. In the Rur catchment, this means recognizing that agricultural areas enter this state first (May–June) and are most sensitive, necessitating early intervention, while forests exhibit delayed but eventually widespread coupling by late summer.

Finally, it is important to contextualize the magnitude of the correlations. Although the optimized correlation (mean $r = 0.354$) remains statistically weak, this reflects the inherently complex and multi-factor nature of vegetation–water interactions in a humid temperate region. This suggests that the relationships are influenced not only by SM but also by atmospheric properties, soil properties, land management practices, and potential lag effects (Leisner et al., 2022; Mehmood et al., 2025; Quetin and Swann, 2017). The critical finding is therefore not the absolute strength of the correlation, but its systematic and significant superiority over the negligible relationship observed in water-replete condition. Future work should extend this framework by integrating additional controls, such as deeper SM layers, evaporative demand, and land management information, to further improve drought localized early-warning capabilities in humid regions.

4.3. Implications for agricultural drought monitoring in the Rur catchment

The findings, from spatiotemporal and severity characterization of drought to SM-vegetation coupling analyses, form a clear and actionable framework for agricultural drought monitoring in a humid temperate catchment like the Rur. In such regions, where water limitation is intermittent rather than constant, effective early warning must move beyond static continental-scale, anomaly-based approaches—such as those used in operational monitoring systems (e.g., European Drought Observatory; European Drought Observatory, E., 2020)—to a locally calibrated, condition-sensitive framework that targets the absolute threshold at which vegetation becomes water-limited.

First, monitoring must be spatially prioritized based on inherent vulnerability. The persistent south–north gradient in baseline SM (Fig. 5) designates the northern agricultural lowlands as inherently drought-sensitive. This is corroborated by VCI dynamics (Fig. 6) and the progression of the "coupling curtain", which reveals that these areas enter a water-limited state earliest (May–June) and sustain the strongest SM–VCI coupling in the peak summer (Fig. 10). Therefore, monitoring resources should be concentrated in the northern lowlands during the early to mid-growing season.

Second, and most critically, effective monitoring is best guided by SM regime. The identification of the 64% nFK threshold provides a crucial operational benchmark. Real-time systems should first diagnose whether conditions are water-limited by comparing observed SM against this threshold. Only when SM $\leq$ 64% nFK does surface SM become a reliable predictor of vegetation stress. This step fundamentally refines monitoring logic by emphasizing periods when monitoring is decision-relevant.

Third, while land cover modulates sensitivity, the SM threshold dictates the relevance of the signal. Under water-limited conditions, agricultural land and grasslands show relatively strongest coupling throughout the growing season, confirming surface SM as an effective early warning indicator, alerting timely signals for irrigation scheduling for shallow-rooted crop types. In contrast, forested areas remain largely decoupled throughout the season due to deeper rooting systems and access to subsurface water; thus, drought monitoring in forests should rely on deeper SM measurements, tree water potential, or species-specific physiological indicators rather than surface SM alone.

This approach optimizes resource allocation by concentrating effort on the most vulnerable areas during the most critical windows. For the Rur catchment, this means (i) using the 64% nFK threshold as a gatekeeper to activate agricultural drought monitoring, (ii) prioritizing the northern croplands from late spring through summer; and (iii) employing land-cover-specific response protocols once water-limited conditions are confirmed. Furthermore, this framework is transferable, while the specific threshold may vary with soil type and climate, the principle of identifying a local SM threshold to trigger monitoring offers a scalable template for improving drought preparedness across humid temperate agricultural regions worldwide.

4.4. Contextual considerations and transferability

It is also important to acknowledge certain contextual factors when interpreting these findings: (i) regarding temporal coverage, the 25-year study period (2000–2024) aligns with nearly the full MODIS record and encompasses multiple major drought events, ensuring that the identified threshold and coupling patterns reflect a broad range of recent hydroclimatic conditions. While at least 30-year baseline is conventionally used for climatological norms (Wright, 2008), our analysis—focused on relative, regime-specific coupling rather than absolute climatic trends—provides a robust foundation for contemporary agricultural drought monitoring. Nevertheless, in a changing climate, the 64% nFK threshold may shift over time due to altered precipitation regimes, warming temperatures, and potential vegetation adaptation. Future monitoring frameworks should therefore periodically recalibrate such thresholds using updated data, ensuring their continued relevance for early warning and agricultural water management in temperate humid regions.

(ii) with respect to regional context, the 64% nFK threshold reflects the integrated soil, vegetation, geomorphological, and climatic characteristics of the Rur catchment, which is representative of humid temperate landscapes. Direct transferability to other areas should be approached with caution, as the optimal threshold may differ substantially under varying climate regimes, soil textures, water-holding capacities, vegetation types, and rooting depths. The primary contribution of this study is therefore not the specific numerical value itself, but the methodological framework for identifying locally relevant thresholds to separate water- and energy-limited regimes. This transferable framework—including data preparation, threshold optimization, stability validation, result visualization and local interpretation—can be applied in other regions using site-specific data, yielding thresholds that reflect local hydroclimatic and ecological conditions. The implementation of this framework is supported by the code scripts provided in the supplementary material, enabling its application and reproducibility. Such recalibration ensures that the relationship between SM and vegetation stress is accurately captured in diverse contexts.

(iii) regarding temporal response dynamics, this study focused on contemporaneous SM–vegetation coupling based on literature indicating rapid shallow-layer responses in humid temperate regions (Na et al., 2021; Tian et al., 2025). Potential lagged relationships of one to two months were therefore not explicitly tested. Future work could investigate such lags, particularly in deeper soil layers or during recovery phases following drought events.

5. Conclusion

This study provides a comprehensive analysis of agricultural drought in the humid temperate Rur catchment by first identifying spatiotemporal patterns of SM and vegetation condition and assessing agricultural drought severity. It then introduced a critical SM threshold (SM $\leq$ 64% nFK) to isolate water-limited periods, under which SM–VCI correlations were quantified and land-cover sensitivity was assessed. This threshold-driven geospatial framework moves beyond conventional growing-season analyses by distinguishing when SM actually limits vegetation in a humid temperate system.

The findings reveal a dynamic “coupling curtain” that progresses seasonally: water-limited conditions emerge first in the northern agricultural lowlands (May–June) and expand catchment-wide by late summer, with coupling strength peaking in August (mean $r = 0.501$). Within this water-limited regime, agricultural land and grassland shows the strongest SM–VCI coupling, while forests remain decoupled due to deeper root systems. These empirical insights demonstrate how agricultural drought sensitivity propagates across a heterogeneous landscape—a direct validation of the regime-separation framework introduced in this study.

By operationalizing vegetation-defined SM thresholds into an operational monitoring tool, this work bridges the gap between theoretical regime separation and practical agricultural drought detection. The resulting framework provides a clear signal for when to shift from routine observation to targeted vigilance in agricultural landscapes, offering a scalable template for improving drought preparedness in humid and temperate agricultural regions worldwide. Future work should investigate the variability of this threshold across soil types, climate regimes, and geomorphological settings, while incorporating deeper SM data to further refine predictive models of agricultural drought stress.

CRediT authorship contribution statement

Abdul Baqi Ahady: Writing – original draft, Visualization, Software, Methodology, Formal analysis, Data curation, Conceptualization. **Stefanie Wolf:** Writing – review & editing, Supervision, Resources, Funding acquisition, Conceptualization. **Elena-Maria Klopries:** Writing – review & editing, Supervision, Resources, Methodology, Funding acquisition, Conceptualization.

Declaration of generative AI and AI-assisted technologies in the writing process

During the preparation of this manuscript, the author(s) used AI tools to assist with language refinement, clarity, and code debugging and troubleshooting. All content and analyses were subsequently reviewed and edited by the author(s), who take full responsibility for the accuracy and integrity of the published work.

Declaration of competing interest

The authors declare that they have no known competing financial interests or personal relationships that could have appeared to influence the work reported in this paper.

Acknowledgement

The first author gratefully acknowledges the scholarship support provided by the German Academic Exchange Service (DAAD). The author also extends sincere thanks to the BMBF DryRiver project (Grant No. FKZ02WEE1628B), for its valuable support, within which part of this work was conducted. Further appreciation is expressed to Prof. Dr.-Ing. Holger Schüttrumpf for his helpful comments on an earlier version of the manuscript, and to the entire leadership of the Institute of Hydraulics and Water Resources Management at RWTH Aachen University for their cooperation and for providing the essential research environment and facilities that supported the completion of this study.

Appendix A

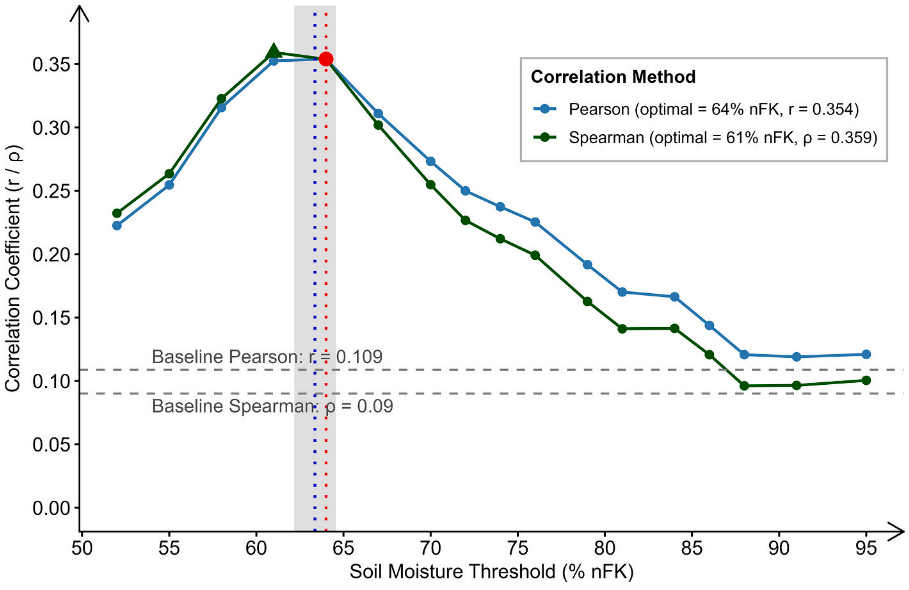

Fig. A1. Comparison of Pearson and Spearman correlation coefficients between SM and VCI as a function of SM threshold. The gray envelope shows ±1.6 SD around the LOO cross-validation mean threshold (63.6 ± 1.6% nFK).

Table A1
Leave-one-year-out cross-validation results showing optimal threshold and correlation for each withheld year (2000–2024).

Left-out Year	Threshold (% nFK)	Pearson Cor. (r)
2000	63.0	0.352
2001	64.0	0.370
2002	63.0	0.352
2003	62.0	0.347
2004	64.0	0.357
2005	64.0	0.355
2006	64.0	0.356
2007	63.0	0.352
2008	63.0	0.352
2009	61.0	0.358
2010	64.0	0.352
2011	65.0	0.356
2012	64.0	0.360
2013	64.0	0.351
2014	64.0	0.352
2015	65.0	0.355
2016	64.0	0.356
2017	65.0	0.359
2018	65.0	0.332
2019	62.0	0.349
2020	62.0	0.343
2021	63.0	0.352
2022	62.0	0.362
2023	61.0	0.371
2024	63.0	0.353

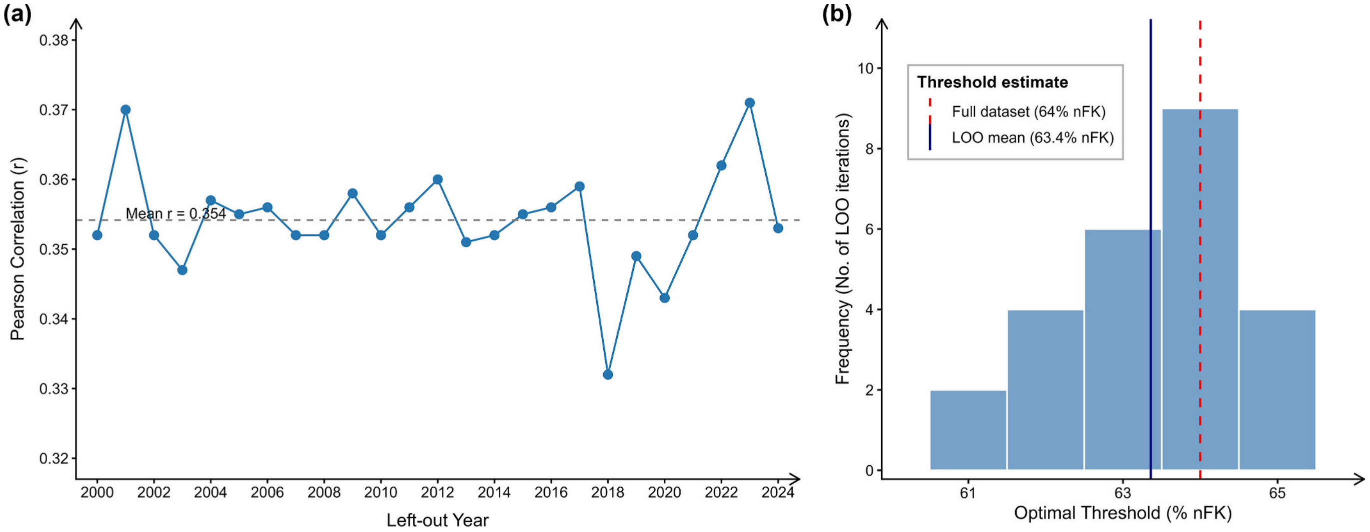

Fig. A2. Threshold stability analysis using LOO cross-validation (2000–2024). (a) variation of Pearson correlation r corresponding to the left-out-year using the threshold optimized on the remaining 24 years. (b) distribution of optimal thresholds from 25 LOO cross-validation iterations. Red line: full-dataset optimum (64% nFK). Blue line: LOO cross-validation mean (63.6% nFK).

Appendix B

Table A2
Temperature anomalies during drought years, distinguishing between phenology-driven and atmosphere-driven conditions.

Year	Spring anomaly (April)	Summer anomaly (July/July-August)	Interpretation
2001	-2.04	+0.26	cold spring, no strong summer heat
2003	−0.51	+1.57	strong summer heat
2006	−1.19	+3.91	extreme summer heat
2018	+3.13	+2.53	strong spring + summer heat
2020	+2.18	+1.19	warm spring and summer
2022	−0.78	+1.76	strong summer heat

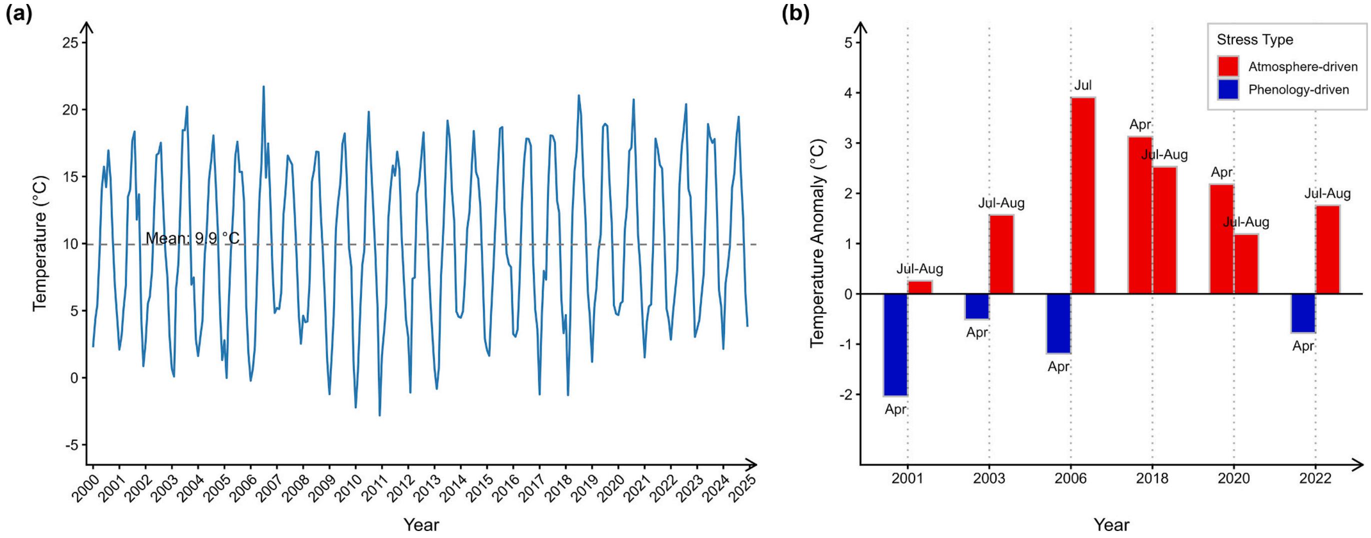

Fig. A3. Temperature characteristics of the Rur catchment (2000–2024). (a) Monthly mean temperatures (steel blue line) with the overall mean temperature (dashed gray line, 9.9 °C). (b) Temperature anomalies during identified drought years. Anomalies are calculated relative to 2000–2024 monthly means. The data were obtained from ERA5-Land monthly averaged reanalysis data (Muñoz Sabater, 2019) and processed in GEE for the Rur catchment.

Appendix. Supplementary data

Supplementary data to this article can be found online at https://doi.org/10.1016/j.ecolind.2026.114875.

Data availability

Data will be made available on request.

References

Ahady, A.B., Klopries, E.-M., Schüttrumpf, H., Wolf, S., 2025. Drought analysis methods: A multidisciplinary review with insights on key decision-making factors in method selection. Water 17 (15), 2248. https://doi.org/10.3390/w17152248.

Ahemd, H.A., Al-Faraj, A.A., Abdel-Ghany, A.M., 2016. Shading greenhouses to improve the microclimate, energy and water saving in hot regions: A review. Sci. Hortic. 201, 36–45. https://doi.org/10.1016/j.scienta.2016.01.030.

Ali, M., Montzka, C., Stadler, A., Menz, G., Thonfeld, F., Vereecken, H., 2015. Estimation and validation of RapidEye-based time-series of leaf area index for winter wheat in the rur catchment (Germany). Remote Sens. 7 (3), 2808–2831. https://doi.org/10.3390/rs70302808.

Bogale, T., Degefa, S., Dalle, G., Abebe, G., 2025. Spatio-temporal variations of drought in the welmel watershed, southeast of Ethiopia using the vegetation condition index and standardized precipitation index. Ecol. Process. 14 (1), 37. https://doi.org/10.1186/s13717-025-00605-0.

Bogena, H., Herbst, M., Hake, J.-F., Kunkel, R., Montzka, C., Pütz, T., Vereecken, H., Wendland, F., 2005. MOSYRUR - Water Balance Analysis in the Rur Basin. Forschungszentrum Jülich GmbH Zentralbibliothek, Verlag.

Bogena, H.r., Montzka, C., Huisman, J.a., Graf, A., Schmidt, M., Stockinger, M., von Hebel, C., Hendricks-Franssen, H.j., van der Kruk, J., Tappe, W., Lücke, A., Baatz, R., Bol, R., Groh, J., Pütz, T., Jakobi, J., Kunkel, R., Sorg, J., Vereecken, H., 2018. The TERENO-Rur hydrological observatory: a multiscale multi-compartment research platform for the advancement of hydrological science. Vadose Zone J. 17 (1), 180055. https://doi.org/10.2136/vzj2018.03.0055.

Burka, A., Biazin, B., Bewket, W., 2024. Spatial drought occurrences and distribution using VCI, TCI, VHI, and google earth engine in bilate river watershed, rift valley of Ethiopia. Geomat. Nat. Haz. Risk 15 (1), 2377672. https://doi.org/10.1080/19475705.2024.2377672.

Denissen, J.M.C., Teuling, A.J., Pitman, A.J., Koirala, S., Migliavacca, M., Li, W., Reichstein, M., Winkler, A.J., Zhan, C., Orth, R., 2022. Widespread shift from ecosystem energy to water limitation with climate change. Nat. Clim. Chang. 12 (7), 677–684. https://doi.org/10.1038/s41558-022-01403-8.

Deutscher Wetterdienst, 2025a. Gridded modeled soil moisture data for Germany. https://cdc.dwd.de/portal/.

Deutscher Wetterdienst, 2025b. Station-based precipitation observations for Germany. https://cdc.dwd.de/portal/.

Didan, K., 2021. MODIS/Terra vegetation indices 16-day l3 global 250m SIN grid v061 | NASA earthdata [dataset]. Earth Sci. Data Systems, NASA. https://doi.org/10.5067/MODIS/MOD13Q1.061.

Dietrich, L., Kahmen, A., 2019. Water relations of drought-stressed temperate trees benefit from short drought-intermitting rainfall events. Agric. For. Meteorol. 265, 70–77. https://doi.org/10.1016/j.agrformet.2018.11.012.

Dogan, S., Berktay, A., Singh, V.P., 2012. Comparison of multi-monthly rainfall-based drought severity indices, with application to semi-arid Konya closed basin, Turkey. J. Hydrol. 470–471, 255–268. https://doi.org/10.1016/j.jhydrol.2012.09.003.

Döscher, N., Ketzler, G., Leuchner, M., 2023. Localising and quantifying night-time cooling effects from sub-catchments in a mid-European low mountain area. Theor. Appl. Climatol. 151 (3), 1855–1870. https://doi.org/10.1007/s00704-023-04360-0.

Du, R., Wu, J., Tian, F., Yang, J., Han, X., Chen, M., Zhao, B., Lin, J., 2023. Reversal of soil moisture constraint on vegetation growth in North China. Sci. Total Environ. 865, 161246. https://doi.org/10.1016/j.scitotenv.2022.161246.

Eingrüber, N., Korres, W., 2022. Climate change simulation and trend analysis of extreme precipitation and floods in the mesoscale rur catchment in western Germany until 2099 using statistical downscaling model (SDSM) and the soil & water assessment tool (SWAT model). Sci. Total Environ. 838, 155775. https://doi.org/10.1016/j.scitotenv.2022.155775.

Esch, S., Korres, W., Reichenau, T.G., Schneider, K., 2018. Soil moisture index from ERS-SAR and its application to the analysis of spatial patterns in agricultural areas. J. Appl. Remote. Sens. 12 (2), 022206. https://doi.org/10.1117/1.JRS.12.022206.

European Drought Observatory, E, 2020. *EDO Combined Drought Indicator (CDI) (version 1.6.1, dismissed)* (Version fe6cd25aec944a708ebe545f7ac3af20) [Dataset]. European Commission, Joint Research Centre. https://doi.org/10.2905/JRC.1BNVE0R.

Feldman, A.F., Short Gianotti, D.J., Trigo, I.F., Salvucci, G.D., Entekhabi, D., 2019. Satellite-based assessment of land surface energy partitioning–soil moisture relationships and effects of confounding variables. Water Resour. Res. 55 (12), 10657–10677. https://doi.org/10.1029/2019WR025874.

Fu, Z., Ciais, P., Feldman, A.F., Gentine, P., Makowski, D., Prentice, I.C., Stoy, P.C., Bastos, A., Wigneron, J.-P., 2022a. Critical soil moisture thresholds of plant water stress in terrestrial ecosystems. Sci. Adv. 8 (44), eabq7827. https://doi.org/10.1126/sciadv.abq7827.

Fu, Z., Ciais, P., Makowski, D., Bastos, A., Stoy, P.C., Ibrom, A., Knohl, A., Migliavacca, M., Cuntz, M., Šigut, L., Peichl, M., Loustau, D., El-Madany, T.S., Buchmann, N., Gharun, M., Janssens, I., Markwitz, C., Grünwald, T., Rebmann, C., Wigneron, J.-P., 2022b. Uncovering the critical soil moisture thresholds of plant water stress for european ecosystems. Glob. Chang. Biol. 28 (6), 2111–2123. https://doi.org/10.1111/gcb.16050.

Gessner, U., Reinermann, S., Asam, S., Kuenzer, C., 2023. Vegetation stress monitor—assessment of drought and temperature-related effects on vegetation in Germany analyzing MODIS time series over 23 years. Remote Sens. 15 (22), 5428. https://doi.org/10.3390/rs15225428.

Ghimire, P., Karki, S., Pandey, V.P., Pradhan, A.M.S., 2025. Mapping spatio-temporal dynamics of irrigated agriculture in Nepal using MODIS NDVI and statistical data with google earth engine: a step towards improved irrigation planning. Int. J. Appl. Earth Obs. Geoinf. 136, 104345. https://doi.org/10.1016/j.jag.2024.104345.

Gogineni, A., Sharma, S., Roy, S., Kumar, P., 2025. Long-term drought analysis and forecasting using hybrid wavelet denoise random forest models with SPI, Z-score, and China Z-index. Arab. J. Sci. Eng. https://doi.org/10.1007/s13369-025-10575-2.

Gorelick, N., Hancher, M., Dixon, M., Ilyushchenko, S., Thau, D., Moore, R., 2017. Google earth engine: planetary-scale geospatial analysis for everyone. Remote Sens. Environ. 202, 18–27. https://doi.org/10.1016/j.rse.2017.06.031.

Hasselquist, N.J., Benegas, L., Roupsard, O., Malmer, A., Ilstedt, U., 2018. Canopy cover effects on local soil water dynamics in a tropical agroforestry system: evaporation drives soil water isotopic enrichment. Hydrol. Process. 32 (8), 994–1004. https://doi.org/10.1002/hyp.11482.

Jiao, W., Wang, L., Smith, W.K., Chang, Q., Wang, H., D'Odorico, P., 2021. Observed increasing water constraint on vegetation growth over the last three decades. Nat. Commun. 12 (1), 3777. https://doi.org/10.1038/s41467-021-24016-9.

Kinzinger, L., Haberstroh, S., Mach, J., Weiler, M., Orlowski, N., Werner, C., 2025. Continuous in-situ water stable isotopes reveal rapid changes in root water uptake by *Fagus sylvatica* during severe drought. Plant Cell Environ. 48 (10), 7627–7639. https://doi.org/10.1111/pce.70055.

Kogan, F.N., 1990. Remote sensing of weather impacts on vegetation in non-homogeneous areas. Int. J. Remote Sens. 11 (8), 1405–1419. https://doi.org/10.1080/01431169008955102.

Korres, W., Reichenau, T.G., Fiener, P., Koyama, C.N., Bogena, H.R., Cornelissen, T., Baatz, R., Herbst, M., Diekkrüger, B., Vereecken, H., Schneider, K., 2015. Spatio-temporal soil moisture patterns – a meta-analysis using plot to catchment scale data. J. Hydrol. 520, 326–341. https://doi.org/10.1016/j.jhydrol.2014.11.042.

Kramm, T., Hoffmeister, D., 2020. Assessing the influence of environmental factors and datasets on soil type prediction with two machine learning algorithms in a heterogeneous area in the rur catchment, Germany. Geoderma Reg. 22, e00316. https://doi.org/10.1016/j.geodrs.2020.e00316.

Kruskal, W.H., Wallis, W.A., 1952. Use of ranks in one-criterion variance analysis. J. Am. Stat. Assoc. 47 (260), 583–621. https://doi.org/10.1080/01621459.1952.10483441.

Lee, J.D., 1973. Statistical and numerical methods of processing examination results by computer. Int. J. Math. Educ. Sci. Technol. 4 (3), 271–278. https://doi.org/10.1080/0020739730040306.

Lehner, B., Grill, G., 2013. Global river hydrography and network routing: baseline data and new approaches to study the world's large river systems. Hydrol. Process. 27 (15), 2171–2186. https://doi.org/10.1002/hyp.9740.

Leisner, C., Potnis, N., Sanz-Saez, A., 2022. Crosstalk and trade-offs: Plant responses to climate change-associated abiotic and biotic stresses. https://www.authorea.com/users/511861/articles/588546-crosstalk-and-trade-offs-plant-responses-to-climate-change-associated-abiotic-and-biotic-stresses?commit=29ffd9345260ead339138561180550d00016bf1c.

Li, S., Sawada, Y., 2022. Soil moisture-vegetation interaction from near-global in-situ soil moisture measurements. Environ. Res. Lett. 17 (11), 114028. https://doi.org/10.1088/1748-9326/ac9c1f.

Li, W., Migliavacca, M., Forkel, M., Denissen, J.M.C., Reichstein, M., Yang, H., Duveiller, G., Weber, U., Orth, R., 2022. Widespread increasing vegetation sensitivity to soil moisture. Nat. Commun. 13 (1), 3959. https://doi.org/10.1038/s41467-022-31667-9.

Li, X., Piao, S., Huntingford, C., Peñuelas, J., Yang, H., Xu, H., Chen, A., Friedlingstein, P., Keenan, T.F., Sitch, S., Wang, X., Zscheischler, J., Mahecha, M.D., 2023. Global variations in critical drought thresholds that impact vegetation. Natl. Sci. Rev. 10 (5), nwad049. https://doi.org/10.1093/nsr/nwad049.

Liang, J., Han, X., Zhou, Y., Yan, L., 2024. Investigating the temporal lag and accumulation effect of climatic factors on vegetation photosynthetic activity over subtropical China. Ecol. Indic. 166, 112406. https://doi.org/10.1016/j.ecolind.2024.112406.

Linke, S., Lehner, B., Ouellet Dallaire, C., Ariwi, J., Grill, G., Anand, M., Beames, P., Burchard-Levine, V., Maxwell, S., Moidu, H., Tan, F., Thieme, M., 2019. Global hydro-environmental sub-basin and river reach characteristics at high spatial resolution. Sci. Data 6 (1), 283. https://doi.org/10.1038/s41597-019-0300-6.

Liu, L., Gudmundsson, L., Hauser, M., Qin, D., Li, S., Seneviratne, S.I., 2020. Soil moisture dominates dryness stress on ecosystem production globally. Nat. Commun. 11 (1), 4892. https://doi.org/10.1038/s41467-020-18631-1.

Liu, Y., Xiao, J., Li, X., Li, Y., 2025. Critical soil moisture detection and water–energy limit shift attribution using satellite-based water and carbon fluxes over China. Hydrol. Earth Syst. Sci. 29 (5), 1241–1258. https://doi.org/10.5194/hess-29-1241-2025.

Luo, M., Meng, F., Sa, C., Duan, Y., Bao, Y., Liu, T., De Maeyer, P., 2021. Response of vegetation phenology to soil moisture dynamics in the mongolian plateau. Catena 206, 105505. https://doi.org/10.1016/j.catena.2021.105505.

Luo, S., Tetzlaff, D., Smith, A., Soulsby, C., 2024. Long-term drought effects on landscape water storage and recovery under contrasting landuses. J. Hydrol. 636, 131339. https://doi.org/10.1016/j.jhydrol.2024.131339.

Mehmood, K., Anees, S.A., Shahzad, F., Muhammad, S., Liu, Q., Khan, W.R., Shah, M., Jamjareegulgarn, P., 2025. Exploring vegetation health in southern Thailand under climate stress from temperature and water impacts between 2000 and 2023. Sci. Rep. 15 (1), 30491. https://doi.org/10.1038/s41598-025-16293-x.

Meng, L., Chambers, J., Koven, C., Pastorello, G., Gimenez, B., Jardine, K., Tang, Y., McDowell, N., Negron-Juarez, R., Longo, M., Araujo, A., Tomasella, J., Fontes, C., Mohan, M., Higuchi, N., 2022. Soil moisture thresholds explain a shift from light-limited to water-limited sap velocity in the central amazon during the 2015–16 el niño drought. Environ. Res. Lett. 17 (6), 064023. https://doi.org/10.1088/1748-9326/ac6f6d.

Mohanty, B.P., Ines, A.V.M., Shin, Y., Gaur, N., Das, N., Jana, R., 2017. A framework for assessing soil moisture deficit and crop water stress at multiple space and time scales under climate change scenarios using model platform, satellite remote sensing, and decision support system. In: Lakshmi, V. (Ed.), Remote Sensing of Hydrological Extremes. Springer International Publishing, pp. 173–196. https://doi.org/10.1007/978-3-319-43744-6_9.

Muñoz Sabater, J., 2019. ERA5-land monthly averaged data from 1950 to present. https://cds.climate.copernicus.eu/datasets/reanalysis-era5-land-monthly-means?tab=overview.

Na, L., Na, R., Bao, Y., Zhang, J., 2021. Time-lagged correlation between soil moisture and intra-annual dynamics of vegetation on the mongolian plateau. Remote Sens. 13 (8), 1527. https://doi.org/10.3390/rs13081527.

Noor, N.M., Noor, N.M., Alias, R., Ideris, M.M., 2020. Drought indices monitoring using SPI and z index score for gua musang, Kelantan. IOP Conf. Ser.: Mater. Sci. Eng. 932 (1), 012050. https://doi.org/10.1088/1757-899X/932/1/012050.

Otkin, J.A., Svoboda, M., Hunt, E.D., Ford, T.W., Anderson, M.C., Hain, C., Basara, J.B., 2018. Flash droughts: A review and assessment of the challenges imposed by rapid-onset droughts in the United States. Bull. Am. Meteorol. Soc. 99 (5), 911–919. https://doi.org/10.1175/BAMS-D-17-0149.1.

Patel, N.R., Chopra, P., Dadhwal, V.K., 2007. Analyzing spatial patterns of meteorological drought using standardized precipitation index. Meteorol. Appl. 14 (4), 329–336. https://doi.org/10.1002/met.33.

Paul, J., 1994. Grenzen der Belastbarkeit die Flüsse Rur (Roer) und Inde im Industriezeitalter. Verl. der Joseph-Kuhl-Ges.

Peters, R.L., Steppe, K., Pappas, C., Zweifel, R., Babst, F., Dietrich, L., von Arx, G., Poyatos, R., Fonti, M., Fonti, P., Grossiord, C., Gharun, M., Buchmann, N., Steger, D. N., Kahmen, A., 2023. Daytime stomatal regulation in mature temperate trees prioritizes stem rehydration at night. New Phytol. 239 (2), 533–546. https://doi.org/10.1111/nph.18964.

Pyka, C., Jacobs, C., Breuer, R., Elbers, J., Nacken, H., Sewilam, H., Timmerman, J., 2016. Effects of water diversion and climate change on the rur and meuse in low-flow situations. Environ. Earth Sci. 75 (16), 1206. https://doi.org/10.1007/s12665-016-5989-3.

Quetin, G.R., Swann, A.L.S., 2017. Empirically derived sensitivity of vegetation to climate across global gradients of temperature and precipitation. J. Clim. 30 (15), 5835–5849. https://doi.org/10.1175/JCLI-D-16-0829.1.

Rebetez, M., Dupont, O., Giroud, M., 2009. An analysis of the july 2006 heatwave extent in europe compared to the record year of 2003. Theor. Appl. Climatol. 95 (1), 1–7. https://doi.org/10.1007/s00704-007-0370-9.

Reichenau, T.G., Korres, W., Montzka, C., Fiener, P., Wilken, F., Stadler, A., Waldhoff, G., Schneider, K., 2016. Spatial heterogeneity of leaf area index (LAI) and its temporal course on arable land: combining field measurements, remote sensing and simulation in a comprehensive data analysis approach (CDAA). PLoS One 11 (7), e0158451. https://doi.org/10.1371/journal.pone.0158451.

Roberts, D.R., Bahn, V., Ciuti, S., Boyce, M.S., Elith, J., Guillera-Arroita, G., Hauenstein, S., Lahoz-Monfort, J.J., Schröder, B., Thuiller, W., Warton, D.I., Wintle, B.A., Hartig, F., Dormann, C.F., 2017. Cross-validation strategies for data with temporal, spatial, hierarchical, or phylogenetic structure. Ecography 40 (8), 913–929. https://doi.org/10.1111/ecog.02881.

Royer, P.D., Breshears, D.D., Zou, C.B., Villegas, J.C., Cobb, N.S., Kurc, S.A., 2012. Density-dependent ecohydrological effects of piñon–Juniper woody canopy cover on soil microclimate and potential soil evaporation. Rangel. Ecol. Manag. 65 (1), 11–20. https://doi.org/10.2111/REM-D-11-00007.1.

Ruichen, M., Jinxi, S., Bin, T., Wenjin, X., Feihe, K., Haotian, S., Yuxin, L., 2023. Vegetation variation regulates soil moisture sensitivity to climate change on the loess plateau. J. Hydrol. 617, 128763. https://doi.org/10.1016/j.jhydrol.2022.128763.

Rukh, S., Sanders, T.G.M., Krüger, I., Schad, T., Bolte, A., 2023. Distinct responses of european beech (*Fagus sylvatica* l.) to drought intensity and length—A review of the impacts of the 2003 and 2018–2019 drought events in central europe. Forests 14 (2), 248. https://doi.org/10.3390/f14020248.

Selzer, T., Schubert, S., 2023. Cover crop water consumption: analysing performance of the agrometeorological model for the calculation of actual evapotranspiration (AMBAV) in a container experiment. J. Agron. Crop Sci. 209 (5), 747–760. https://doi.org/10.1111/jac.12656.

Seneviratne, S.I., Corti, T., Davin, E.L., Hirschi, M., Jaeger, E.B., Lehner, I., Orlowsky, B., Teuling, A.J., 2010. Investigating soil moisture–climate interactions in a changing climate: A review. Earth Sci. Rev. 99 (3), 125–161. https://doi.org/10.1016/j.earscirev.2010.02.004.

Shukla, S., Meshesha, T.W., Sen, I.S., Bol, R., Bogena, H., Wang, J., 2023. Assessing impacts of land use and land cover (LULC) change on stream flow and runoff in rur basin, Germany. Sustainability 15 (12), 9811. https://doi.org/10.3390/su15129811.

Sodoge, J., Kuhlicke, C., Mahecha, M.D., de Brito, M.M., 2024. Text mining uncovers the unique dynamics of socio-economic impacts of the 2018–2022 multi-year drought in Germany. Nat. Hazards Earth Syst. Sci. 24 (5), 1757–1777. https://doi.org/10.5194/nhess-24-1757-2024.

Stocker, B.D., Zscheischler, J., Keenan, T.F., Prentice, I.C., Peñuelas, J., Seneviratne, S.I., 2018. Quantifying soil moisture impacts on light use efficiency across biomes. New Phytol. 218 (4), 1430–1449. https://doi.org/10.1111/nph.15123.

Stone, M., 1974. Cross-validation and multinomial prediction. Biometrika 61 (3), 509–515. https://doi.org/10.2307/2334733.

Struzewska, J., Kaminski, J.W., 2008. Formation and transport of photooxidants over europe during the july 2006 heat wave – observations and GEM-AQ model simulations. Atmos. Chem. Phys. 8 (3), 721–736. https://doi.org/10.5194/acp-8-721-2008.

Taheri Qazvini, A., Carrion, D., 2023. A spatiotemporal drought analysis application implemented in the google earth engine and applied to Iran as a case study. Remote Sens. 15 (9), 2218. https://doi.org/10.3390/rs15092218.

Teuling, A.J., Seneviratne, S.I., Williams, C., Troch, P.A., 2006. Observed timescales of evapotranspiration response to soil moisture. Geophys. Res. Lett. 33 (23). https://doi.org/10.1029/2006GL028178.

Tian, J., Zhang, B., He, C., Han, Z., Bogena, H.R., Huisman, J.A., 2019. Dynamic response patterns of profile soil moisture wetting events under different land covers in the mountainous area of the Heihe river watershed, Northwest China. Agric. For. Meteorol. 271, 225–239. https://doi.org/10.1016/j.agrformet.2019.03.006.

Tian, R., Li, J., Zheng, J., Liu, L., Han, W., Liu, Y., 2025. Changes in vegetation phenology and its response to different layers of soil moisture in the dry zone of central asia, 1982–2022. J. Hydrol. 646, 132314. https://doi.org/10.1016/j.jhydrol.2024.132314.

van der Breggen, N.N., Hudson, P.F., 2024. Influence of atmospheric rivers on extreme rainfall and high streamflow events in northwestern europe: Rur (roer) river basin. J. Hydrol.: Regional Stud. 51, 101644. https://doi.org/10.1016/j.ejrh.2023.101644.

van Hateren, T.C., Chini, M., Matgen, P., Teuling, A.J., 2021. Ambiguous agricultural drought: characterising soil moisture and vegetation droughts in europe from earth observation. Remote Sens. 13 (10), 1990. https://doi.org/10.3390/rs13101990.

Vidaurre, R., 2019. Drought governance in the Eifel-Rur region. In: Facing Hydrometeorological Extreme Events. John Wiley & Sons, Ltd, pp. 233–244. https://doi.org/10.1002/9781119383567.ch16.

Waldhoff, G., Lussem, U., Bareth, G., 2017. Multi-data approach for remote sensing-based regional crop rotation mapping: A case study for the rur catchment, Germany. Int. J. Appl. Earth Obs. Geoinf. 61, 55–69. https://doi.org/10.1016/j.jag.2017.04.009.

Wang, X., Wang, B., Xu, X., Liu, T., Duan, Y., Zhao, Y., 2018. Spatial and temporal variations in surface soil moisture and vegetation cover in the loess plateau from 2000 to 2015. Ecol. Indic. 95, 320–330. https://doi.org/10.1016/j.ecolind.2018.07.058.

Wang, Y., Rammig, A., Blickensdörfer, L., Wang, Y., Zhu, X.X., Buras, A., 2025. Species-specific responses of canopy greenness to the extreme droughts of 2018 and 2022 for four abundant tree species in Germany. Sci. Total Environ. 958, 177938. https://doi.org/10.1016/j.scitotenv.2024.177938.

Wei, X., Huang, Q., Huang, S., Leng, G., Qu, Y., Deng, M., Han, Z., Zhao, J., Liu, D., Bai, Q., 2022. Assessing the feedback relationship between vegetation and soil moisture over the loess plateau, China. Ecol. Indic. 134, 108493. https://doi.org/10.1016/j.ecolind.2021.108493.

West, H., Quinn, N., Horswell, M., White, P., 2018. Assessing vegetation response to soil moisture fluctuation under extreme drought using sentinel-2. Water 10 (7), 838. https://doi.org/10.3390/w10070838.

Westerkamp, C., Thünemann, C., Schaarschmidt, M., 2024. Model for the calculation of soil compaction on agricultural land, pp. 455–460. https://dl.gi.de/handle/20.500.12116/43920.

Wilhite, D., Glantz, M., 1985. Understanding the Drought Phenomenon: The Role of Definitions. National Drought Mitigation Center: Faculty Publications. https://digitalcommons.unl.edu/droughtfacpub/20.

Wolf, S.S., Schüttrumpf, H., Lehmkuhl, F., 2023a. The long-term-memory of a typical mid-European upland to lowland river: Or why we struggle to reach a good ecological state for our rivers (überarbeitete Auflage). RWTH Aachen University; Online. https://publications.rwth-aachen.de/record/959646.

Wolf, S., Stenger, D., Steudtner, F., Esser, V., Lehmkuhl, F., Schüttrumpf, H., 2023b. Modeling anthropogenic affected sediment transport in a mid-sized european river catchment–extension of the sediment rating curve equation. Modeling Earth Syst. Environ. 9 (4), 3815–3835. https://doi.org/10.1007/s40808-023-01703-8.

Wright, W., 2008. Observing the climate—challenges for the 21st century. World meteorological Organization. https://wmo.int/media/magazine-article/observing-climate-challenges-21st-century.

Wu, Y., Bachmann, D., Schüttrumpf, H., 2025. Long-term hydrodynamic modeling of low-flow conditions with groundwater–river interaction: case study of the Rur River. Hydrology 12 (10), 270. https://doi.org/10.3390/hydrology12100270.

Yang, X., Zhang, Z., Guan, Q., Zhang, E., Sun, Y., Yan, Y., Du, Q., 2023. Coupling mechanism between vegetation and multi-depth soil moisture in arid–semiarid area: shift of dominant role from vegetation to soil moisture. For. Ecol. Manag. 546, 121323. https://doi.org/10.1016/j.foreco.2023.121323.

Zhang, L., Jiao, W., Zhang, H., Huang, C., Tong, Q., 2017. Studying drought phenomena in the continental United States in 2011 and 2012 using various drought indices. Remote Sens. Environ. 190, 96–106. https://doi.org/10.1016/j.rse.2016.12.010.

Zhang, W., Wei, F., Horion, S., Fensholt, R., Forkel, M., Brandt, M., 2022. Global quantification of the bidirectional dependency between soil moisture and vegetation productivity. Agric. For. Meteorol. 313, 108735. https://doi.org/10.1016/j.agrformet.2021.108735.

Zuo, Z., Qiao, L., Zhang, R., Chen, D., Piao, S., Xiao, D., Zhang, K., 2024. Importance of soil moisture conservation in mitigating climate change. Sci. Bull. 69 (9), 1332–1341. https://doi.org/10.1016/j.scib.2024.02.033.